An experimental study of sepiolite dissolution and growth rates as function of the aqueous solution saturation state at 60 °C

Josesphina J P A Mulders, Eric H Oelkers

An experimental study of sepiolite dissolution and growth rates as function of the aqueous solution saturation state at 60 °C

Josesphina J.P.A. Mulders[a], Eric. H. Oelkers[b]

[a]*Earth Sciences, University College London, Gower Street, WC1E 6BT, London, United Kingdom*

[b]*GET-Université de Toulouse-CNRS-IRD-OMP, 14 Avenue Edouard Belin, 31400 Toulouse, France*

Abstract

Clay mineral growth can directly affect the chemistry and permeability of many natural systems, including soils, marine sediments, Earth surface waters, geothermal powerplants and carbon dioxide storage sites. Notably, the sluggish precipitation of clay minerals has been hypothesised to hinder Earth surface weathering rates. To date, there are limited data on the rate of clay mineral growth and on the effect of the aqueous solution saturation states on these rates. In this study we quantify the growth and dissolution rates of sepiolite, a 2:1 layered Mg-phyllosilicate ($Mg_4Si_6O_{15}(OH)_2*6H_2O$) as a function of aqueous solution saturation state in a series of mixed flow experiments. Results of the both the dissolution and growth experiments are consistent with $r = -10^{-14.80}\left(1 - \exp\left(\frac{\Delta G_r}{\sigma RT}\right)\right)$, where r refers to the surface area normalized growth rate of sepiolite in units of mol/cm^2/s, ΔG_r denotes Gibbs Free energy of the sepiolite dissolution reaction, which is <0 for undersaturated solutions, 0 at equilibrium and >0 for supersaturated solutions, σ refers to Temkin's stoichiometric number, R stands for the gas constant and T symbolizes absolute temperature. This rate equation suggests that sepiolite dissolution and growth are consistent with transition state theory and the concept of micro-reversibility. The relative decrease in aqueous Mg^{2+} and Si concentrations in the outlet aqueous solutions of the experiments, and the X-Ray diffraction patterns of the precipitates collected from the experiments, confirm the growth of crystalline sepiolite. The results of longer-term experiments suggest that sepiolite growth rates decrease over time. Such a decrease in the growth rate has been associated with poisoning or destruction of the

sepiolite reactive surface sites. Calculations of sepiolite growth coupled to either forsterite or enstatite dissolution, based on laboratory measured rates suggest that the dissolution of the primary mineral is the rate-limiting step during the weathering of most natural systems. These results, however, contradict the saturation states of natural fluids such as observed in Icelandic waters, where clays are strongly supersaturated, whilst primary phases are relatively close to equilibrium. This discrepancy may be due to the consumption of reactive sites over time such that clay mineral precipitation rates in most natural systems are controlled by the relative slow nucleation rates of new reactive sites on the clay mineral surface.

1. Introduction

The reactivity of clay minerals plays a critical role on the chemistry and permeability of many natural systems (c.f. Chamley, 2013; Hendricks and Fry, 1930; Pauling, 1930). The transport of clay minerals provides nutrients to the oceans, via selective desorption of nutrients initially adsorbed on clay mineral particles (c.f. Avnimelech and McHenry, 1984). Clay minerals attenuate contaminant transport in groundwater environments by providing surfaces for adsorption and by forming impermeable barriers in the subsurface (c.f. Katsumi et al., 2010; Malusis et al., 2003; Misaelides, 2019). Clay mineral nucleation and growth can decrease the porosity and permeability of geothermal systems and subsurface CO_2 storage sites (c.f. Shafizadeh et al., 2020; Shao et al., 2010). Such processes could lower the efficiency of CO_2 storage and decrease the harvesting potential of geothermal energy. Conversely, clay mineral dissolution can provide the divalent metals necessary for CO_2 sequestration (Harrison et al., 2012; Mulders and Oelkers, 2020; Thom et al., 2013).

The slow precipitation of authigenic clays has been speculated to be the rate limiting step in weathering reactions (Maher et al., 2009; Zhu and Lu, 2009). Weathering is one of the key feedback mechanisms in the global carbon cycle, as aqueous bicarbonate ions are formed during primary rock dissolution and subsequently transported to the oceans, where they are deposited as carbonate

minerals (c.f. Berner, 1964, 1992). As mineral dissolution is slowed when the aqueous concentrations of the mineral components increase in solution resulting in lower degrees of undersaturation (e.g. Oelkers, 2001a; Schott et al., 2009), slow secondary mineral precipitation could limit the rates of primary rock dissolution.

Despite the abundance of authigenic clays in natural environments, it has proven challenging to quantify clay mineral precipitation rates in the laboratory (Hindshaw et al., 2019; Linares and Huertas, 1971). Typically, attempts to precipitate Al-rich clays from highly supersaturated conditions in the laboratory has resulted in the formation of poorly crystalline clay-like phases and/or the co-precipitation of Al-(hydr)oxides (Hem and Lind, 1974; Linares and Huertas, 1971; Nagy and Lasaga, 1992; Van Oosterwyck-Gastuche and La Iglesia, 1978). Yang and Steefel (2008), however, reported the growth rates of crystalline kaolinite. In contrast, some Mg-silicate clays can be readily precipitated in the laboratory at ambient conditions (Arizaleta et al., 2020).

Several studies have reported on the nucleation, growth and dissolution of sepiolite (Arizaleta et al., 2020; Baldermann et al., 2018; Mulders et al., 2018; Mulders and Oelkers, 2020; Tosca and Masterson, 2014; Tutolo and Tosca, 2018; Wollast et al., 1968), a 2:1 layered Mg-phyllosilicate ($Mg_4Si_6O_{15}(OH)_2*6H_2O$) characterized by its continuous inverted tetrahedral sheets and discontinuous octahedral sheets. Sepiolite is found in volcanic sediments, silicious lake sediments, and it has been inferred to precipitate in the subsurface carbon storage site near the Hellisheiði geothermal powerplant in Iceland (Bowles et al., 1971; Gislason et al., 2010; Perraki and Orfanoudaki, 2008; Stoessell and Hay, 1978; Tutolo and Tosca, 2018). Most past experimental studies on sepiolite precipitation have only considered highly supersaturated conditions. At such conditions rates are fast and the nucleation of amorphous sepiolite-like phases is favoured (c.f. Baldermann et al., 2018; Tosca and Masterson, 2014). Such amorphous phases can recrystallize to more stable crystalline phases over time, yet Che et al. (2021) reported that amorphous Mg-silicate phases can persist at near to equilibrium conditions over substantial time frames at ambient

temperature. Natural systems, however, are often closer to equilibrium with respect to precipitating and dissolving phases (Bénézeth et al., 2008). At such conditions, rates are slower and precipitation can proceed via nucleation and growth on pre-existing surfaces, rather than via the spontaneous nucleation of amorphous phases from solution followed by crystallization (De Yoreo and Vekilov, 2003). Critically, at near to equilibrium conditions kinetic barriers can hinder the nucleation of stable secondary phases via either mechanism.

To date, there is one study reporting the growth of sepiolite as a function of aqueous solution saturation state (Arizaleta et al., 2020). This study grew sepiolite in seeded batch experiments at ambient temperature conditions. The pH of their reactive aqueous solutions ranged between 9-10 and the sepiolite saturation indices ranged between 3.21 and 16.40. Although this study provides insight into sepiolite growth rates, the batch reactor approach does not allow for the accurate determination of these rates at fixed solution saturation states and aqueous compositions, as aqueous concentrations continuously change over time (c.f. Oelkers et al., 2001).

The relationship between sepiolite dissolution and growth mechanisms as a function of solution saturation state has yet to be studied, but several studies have explored this relationship in other clay mineral systems. Nagy et al. (1991) investigated the dependency of kaolinite, a 1:1 layered Al-phyllosilicate, dissolution and growth rates as a function of reaction affinity at 80 ^{o}C. The authors found a linear relationship between the reaction rate and the ion activity product during the initial phase of mineral growth. A linear dependency of the dissolution and growth rates on the ion activity product of the reaction has also been observed for brucite, boehmite and gibbsite, and can be quantified within the framework of transition state theory (Bénézeth et al., 2008; Pokrovsky and Schott, 2004). Nagy et al. (1991) observed that over time the precipitation rate of kaolinite decreased and the relationship between the ion activity product and the reaction rate became non-linear. The authors attributed this non-linearity to a decrease in the number of reactive surface sites available on the kaolinite surface, and interpreted longer-term rates within the framework of the

Burton, Cabrera and Frank (BCF) two-dimensional growth model (Burton et al., 1951). Measuring sepiolite dissolution and growth rates as a function of its ion activity product and time allows us to assess the link between its dissolution and growth rates, and to test and generalize the Nagy et al. (1991) model for clay mineral growth and dissolution.

The motivation for this study is thus three-fold: (i) to quantify the dissolution and growth rates of sepiolite as a function of its ion activity product, (ii) to formulate a generalized mechanism for clay mineral dissolution and growth and (iii) to assess the potential of slow mineral growth rates as the rate limiting step during weathering.

2. Theoretical background

Sepiolite dissolution and precipitation can been described by (Stoessell, 1988):

$$Mg_4Si_6O_{15}(OH)_2 \cdot 6H_2O + 8H^+ \leftrightarrow 4Mg^{2+} + 6SiO_2(aq) + 11H_2O \quad (1)$$

The standard state adopted in this study for aqueous solutes is that of unit activity of the species in a hypothetical 1 molal solution at infinite dilution at any temperature and pressure. The standard state of H_2O and pure minerals are taken to be 1. Taking account of these standard states, the law of mass action relating the aqueous activities of magnesium, silica and protons in equilibrium with sepiolite is given by:

$$K_{sp} = \frac{a_{H^+}^8}{a_{Mg^{2+}}^4 \, a_{SiO_2}^6} \quad (2)$$

where K_{sp} stands for the solubility product or equilibrium constant of sepiolite and a_i represents the activity of the subscripted species. The ion activation product (IAP) is defined as the product of the activities of any aqueous solution, e.g. the righthand side of Eq. 2, which may or may not be at equilibrium with sepiolite.

Several studies have explored the thermodynamic properties of reaction 1 (Baldermann et al., 2018; Christ et al., 1973; Kent and Kastner, 1985; Stoessell, 1988; Wolery and Jarek, 2003). Christ et al. (1973) and Stoessell (1988) determined the equilibrium constant of sepiolite from a series of batch experiments at a pressure of 1 bar and at temperatures ranging from 25 to 90 °C. Equilibrium constants for reaction 1 determined from the thermodynamic data of sepiolite and that of aqueous Mg^{2+}, SiO_2 and H^+ (Helgeson and Kirkham, 1976; Walther and Helgeson, 1977) are in close agreement with the experimental results of Christ et al. (1973) and Stoessell (1988) (Helgeson et al., 1978). The K_{sp} at a temperature of 60 °C and 1 bar pressure was reported to be $10^{27.66}$ (Christ et al., 1973; Helgeson and Kirkham, 1976; Stoessell, 1988). These values are slighlty higher than the K_{sp} of $10^{27.17}$ modelled for an ideal sepiolite at 60 °C by Wolery and Jove-Colon (2004).

Surface area normalized mineral dissolution and growth rates, r, are commonly described using

$$r = k\, e^{-E_a/RT} \prod_i a_i^{n_i} f(\Delta G_r) \qquad (3)$$

where k defines a rate constant, which is a function of pressure and temperature, E_a signifies the activation energy, R represents the gas constant, T refers to absolute temperature, a_i again stands for the activity of the *i*th aqueous species, n_i designates a reaction order and ΔG_r corresponds to the Gibbs free energy of the reaction ($\Delta G_r = RTln(IAP/K_{sepiolite})$) (Lasaga, 1995). Note the Gibbs free energy of the reaction as defined here, is also commonly referred to as the chemical affinity of the reaction. The function $f(\Delta G_r)$ accounts for the variation of the rates as chemical equilibrium is approached. The form of $f(\Delta G_r)$ and the reaction orders, n_i, depend on the dissolution and growth mechanism of the mineral (Oelkers, 2001).

The form of $f(\Delta G_r)$ can be quantified via transition state theory (TST). TST provides a framework to describe mineral dissolution and growth rates and relies on two assumptions: (i) reactants have to pass an energy barrier to yield products and (ii) mineral dissolution and growth is driven by the same elementary reaction on the mineral surface (Eyring, 1938). When dissolution and growth mechanisms follow TST, $f(\Delta G_r)$ is defined as:

147 $$f(\Delta G_r) = 1 - \exp\left(\frac{\Delta G_r}{\sigma RT}\right) \quad (4)$$

148 where σ is Temkin's stoichiometric number, which equals the ratio between the rate of
149 destruction/formation of the activated complex to the overall reaction rate (Schott et al., 2009).
150 Combining Equations (3) and (4) leads at constant temperature to

151 $$r = r_+(1 - \exp\left(\frac{\Delta G_r}{\sigma RT}\right)) \quad (5)$$

152 where the forward reaction (r_+) is defined as:

153 $$r_+ = k_+ \prod_i a_i^{n_i} \quad (6)$$

154 where k_+ is defined as the rate constant of the forward reaction, which itself depends on
155 temperature. Equation (5) and its variants have been successfully applied in mineral dissolution and
156 precipitation rate studies (Arvidson and Luttge, 2010; Beig and Lüttge, 2006; Brantley, 2008; Burch et
157 al., 1993; Hellmann and Tisserand, 2006; Lasaga, 1995; Oelkers et al., 1994; Oelkers and Schott,
158 1995; Schott et al., 2009). Note that alternative rate equations appear to be necessary to describe
159 mineral precipitation rates controlled by the nucleation of 2-dimensional islands on the mineral
160 surface (c.f. Jiang and Tosca, 2020; Saldi et al., 2009; Teng et al., 2000). Two-dimensional islands
161 refer to growth features where a monolayer nucleates and subsequently extents on a pre-existing
162 mineral surface.

163 In this study, the degree of saturation of the aqueous solution is quantified using either the
164 chemical affinity ($A = \Delta G_r$) of the reaction or the solution saturation index. The solution saturation
165 index, *SI*, is defined as:

166 $$SI = \log\left(\frac{IAP}{K_{sepiolite}}\right) = \log\left(e^{-\Delta G_r/RT}\right) = \log\left(e^{-\Delta A/RT}\right) \quad (7)$$

167 where IAP again refers to the ion activation product of the reaction.

168

3. Methods

3.1. Sepiolite

The Valdemore, Spain sepiolite sample used in this study was obtained from the Clay Mineral Society. Preparation of the sample has previously been described in Mulders and Oelkers (2020). The BET surface of the sample was measured using the Brunauer-Emmett Teller (BET) method (Brunauer et al., 1938) and was determined to be 214.0 ±10% m^2/gm from N_2 adsorption measurements using a DIN-ISO 9277. X-ray diffraction (XRD) analyses of this sample using a PANanalytical, X'pfer PRO MPD and Co K(α) radiation, resulted in a diffractogram identical to that of sepiolite as reported by Brindley (1959). This confirmed that the sample was pure sepiolite and that any impurities were below the detection limit (<2 vol.% of the total sample) (Figure 4). XRD data were not background corrected to facilitate assessment of potential silica polymerization in the sepiolite growth experiments. The molar Si:Mg ratio of the sepiolite sample was obtained by micro X-Ray Fluorescence measurements (XRF) (PANalytical PW 2404). The chemical formula of the sepiolite sample was consistent with $Mg_{3.34}Si_6O_{15}(OH)_{0.68}\cdot 6H_2O$. No other elements were found in the solid within the detection limits of this analysis (10-100 µg/g, depending on the analysed element). The Mg/Si ratio of this sepiolite powder is lower than that published by the Clay Mineral database, but is similar to that of Arizaleta et al. (2020), who reported a molar Si/Mg ratio of 1.75.

3.2. Shorter-term flow through dissolution and growth experiments

Sepiolite growth and dissolution rates were determined from a series of mixed flow reactor experiments, as described by Oelkers and Schott (2001). Experiments were performed in either a 160 mL or a 100 mL Teflon flow through reactor, fitted with two openings that allowed for continuous flow of reactive fluids through the reactor (Fig. 1). An inlet aqueous solution was pumped through the reactor with a Gislon minipuls 3 pump, which allows for a wide range of fluid flow rates. Sepiolite was contained in the reactor within 12-14 kD Visking dialyses tubes fitted with two floating

194 closures. To the dialyses tube a slurry of sepiolite was added, which was prepared from 0.8-1 gram
195 of sepiolite and 3 mL of inlet aqueous solution.

196 For the growth experiments, a supersaturated inlet solution was prepared by adding reagent
197 grade sodium metasilicate ($Na_2SiO_3 \cdot 9H_2O$) and magnesium chloride tetrahydrate ($MgCl_2 * 3H_2O$) to
198 deionized water. The composition of each inlet solution is given in Table 1. Note that the molar Mg
199 to Si ratios of the inlet solutions are similar that of the solid sepiolite used in the experiments. The
200 pH of the reactive solution for the growth experiments was adjusted using 1M HCl to obtain a pH of
201 approximately 9.30 and the ionic strength of the solution was fixed to 0.02 M by adding reagent
202 grade NaCl. This pH and ionic strength were chosen both to match our previously reported sepiolite
203 dissolution rates and to allow for the precipitation of sepiolite while avoiding the precipitation of
204 other phases. The identity of the chemical reagents used in the experiments was chosen to minimize
205 any potential effects of the presence of trace ions on measured rates. To ensure that the pH of the
206 inlet solution remained constant over time, the headspace of the sack containing the inlet solution
207 was filled with N_2-gas, preventing the dissolution of atmospheric CO_2 into the fluid, which could
208 result in a pH decrease. To vary the saturation states of the reactive aqueous solution in contact with
209 the sepiolite seed material the fluid flow rates were varied, so that the saturation state of the outlet
210 solution was higher when the flow rate was faster. These shorter-term precipitation experiments
211 were run for 2 to 23 days depending on the flow rate of the inlet aqueous solution. The
212 reproducibility of these shorter-term experiments was assessed by performing each experiment in
213 duplicate. Steady-state was verified by observing a constant aqueous Si concentrations over time in
214 outlet fluid samples collected over 3 to 8 residence times depending on the experiment. The
215 residence time is defined as the volume divided by the fluid flow rate. To verify that the Mg^{2+} and Si
216 concentrations in the inlet solution remained constant during each growth experiment, samples of
217 the inlet solution were collected and analysed at preselected times.

Sepiolite dissolution rates as a function of aqueous solution saturation state were measured in the same flow through reactor system. The pH of the inlet aqueous solutions of these experiments were buffered with NH_4Cl and 28% NH_3 to ensure that the pH of the dissolution experiments corresponded to that of the outlet solution of the sepiolite growth experiments (Table 1). The saturation states during these dissolution experiments was varied by (i) varying the flow rate of the reactive inlet solution and (ii) by varying the concentrations of Si and Mg in the inlet solution by adding sodium metasilicate ($Na_2SiO_3 \cdot 9H_2O$) and magnesium chloride tetrahydrate ($MgCl_2 * 3H_2O$). The compositions of all reactive inlet solutions are reported in Table 1.

The aqueous Si concentrations of fluids collected during the growth and dissolution experiments were measured using a segmented flow analyser (AA3 HR SEAL), which relies on the colorimetric molybdate blue method (Strickland and Parsons, 1972). The calibration of this method was matrix matched during each measurement. To further validate the accuracy of the molybdate blue method, some fluid samples were also analysed by inductively coupled plasma – optical emission spectroscopy (ICP-OES) using a Varian 720 ES. No differences were observed between the results of the ICP-OES analyses and those of the colorimetric molybdate blue method, confirming the validity of the latter method. The uncertainty of the Si measurements is 2%, the detection limit of this method was 0.01 ppm. Aqueous Mg concentrations were obtained from ICP-OES. The uncertainty of the Mg measurements is 2.5% and the detection limit of 0.05 ppm. From the measured change in the aqueous Si and Mg concentrations the dissolution and growth rates were computed using:

$$r = \frac{-\Delta m_i * F}{v_i * SSA * M} \quad (8)$$

where Δm_i designates to the change in concentration of the *i*th element between the inlet and outlet solution at steady state, *F* denotes the fluid flow rate during the experiment, v_i refers to the stoichiometric number of moles of element *i* in the precipitating or dissolving sepiolite, *SSA* represents the BET specific surface area of the initial sepiolite and *M* the mass of sepiolite initially

present in the reactor. The negative sign in Eqn. (8) yields positive rates for precipitation but negative rates for dissolution.

3.3. Longer-term sepiolite growth experiments

To confirm the growth of crystalline sepiolite on the seed material in the flow through experiments, a duplicate series of longer-term experiments ran for over a period of 2.5 months. These experiments were run in a 100 mL Teflon flow through reactor by first adding 0.3 g of sepiolite to 3mL of inlet solution to form the slurry, which was added to the dialyses tube. The fluid flow rate in these experiments was set equal to that of the shorter-term growth experiments performed at the highest aqueous outlet solution saturation state (experiment P-6). This allowed for a relatively high aqueous solution saturation state in the reactor leading to relatively fast sepiolite growth rates. The small amount of sepiolite added, in conjunction with the relatively fast growth rates, allowed for sufficient growth such that the crystallinity of newly grown sepiolite could be confirmed via XRD analyses. The mass of newly precipitated material in the experiments was calculated from:

$$w_P = r \quad * SSA * M * t * MW \tag{9}$$

where, w_P stands for the mass of the precipitate, M represents the mass of sepiolite in the flow through reactor, t refers to the experiment duration and MW denotes the molecular weight of sepiolite. The reaction products of the longer-term growth experiments were collected using a vacuum-filtration system, where the suspension in the dialysis tube was flushed with ethanol. The solid samples were imaged using a Jeol JSM-6480LV high-performance scanning electron microscopy (SEM) and analysed using XRD.

4. Results

4.1. Shorter term growth experiments

Figure 2 shows a representative example of the temporal evolution of outlet aqueous fluid compositions during a shorter-term sepiolite growth experiment (Exp. P-6). After an initial rapid decline in the aqueous Si and Mg^{2+} concentrations and the outlet fluid pH, the concentrations stabilize and remain constant over time indicative of steady-state. Note that the temporal evolution of the Si and Mg^{2+} concentrations and the pH in the duplicate experiments follow similar trends. The similarity between the duplicate samples confirms that the growth experiments are reproducible. There is no notable change in the pH in the inlet fluid over time (Figure 2). This observation suggests that the dissolution of atmospheric CO_2(g) in the alkaline inlet solution was limited by the addition of N_2(g) to the headspace of the bottle. Up to 34 mg of sepiolite precipitated during these short-term experiments.

Evidence for sepiolite precipitation in the shorter-term flow through experiments is provided by the ratio between measured change in the aqueous fluid Si and Mg concentrations between the inlet and outlet solutions, ΔSi and ΔMg, respectively. The ΔSi /ΔMg ratio is close to the Si/Mg ratio of crystalline sepiolite, as indicated by Figure 2 and Table 2. Note that in experiment P-1, the ΔSi/ΔMg ratio is 0.99 and thus differs from the sepiolite Si/Mg ratio of 1.5. Brucite is supersaturated in the experimental outlet solution of experiment P-1. Previous studies have shown that brucite growth at 60 °C is favourable (Pokrovsky and Schott, 2004). Hence, aqueous Mg in experiment P-1 is likely consumed by both brucite and sepiolite precipitation. The rate of sepiolite precipitation is therefore computed only from the rate of aqueous Si consumption in this experiment.

PHREEQC calculations further indicated that aside from sepiolite, anthophyllite, forsterite, chrysotile, kerolite and talc are supersaturated in the many of the reactive outlet solutions in the shorter-term precipitation experiments (see Table 2). Despite the thermodynamic favourability for the precipitation of chrysotile and talc, their formation is kinetically hindered at the temperatures of

289 the experiments considered in this (c.f. Tosca et al., 2011). Kerolite ($(Mg,Ni)_3Si_4O_{10}(OH)_2 \cdot H_2O$),
290 however, is similar in structure and chemical composition to sepiolite and has been observed to
291 precipitate at ambient pressures and temperatures (e.g. Bentz and Peterson, 2020). However, the
292 results of the solid analyses of the longer-term flow through experiments, showed no evidence for
293 the kerolite precipitation (Figure 4). We therefore hypothesise that although the precipitation of
294 kerolite cannot be excluded, the contribution of kerolite to the total precipitate is insignificant.

295

296 ***4.2. Longer-term growth experiments***

297 The longer-term sepiolite flow through precipitation experiments provide further evidence for
298 sepiolite growth. Figures 3 and 4 show the results of these experiments. The general trend in the
299 temporal evolution of aqueous Mg^{2+} and Si concentration of the outlet fluids follows that observed
300 during the shorter-term sepiolite precipitation experiments. However, over time the aqueous Mg^{2+}
301 and Si concentrations increase in the outlet aqueous solutions, while the molar Si/Mg ratio remains
302 relatively constant. Some of the increase in aqueous Mg^{2+} and Si concentrations in the outlet
303 solution coincides with the increase in Mg and Si concentrations in the inlet solution and is
304 associated with the replenishment of the inlet solution as the solution started to run out halfway
305 through the experiment. The concentrations in the second inlet solution were slightly higher
306 compared to those of the first inlet solution. However, the increase in the aqueous Mg^{2+} and Si
307 concentrations in the outlet solution is greater than the corresponding increase in the aqueous Mg^{2+}
308 and Si concentrations in the inlet solution suggesting the slowing of rates over time.

309 From the average growth rate in the longer-term experiments, computed from Eq. 4, the total
310 weight of newly formed precipitate was calculated using Eq. 9. During the longer-term growth
311 experiments, 0.14 g of sepiolite precipitated, amounting to a total of 32 wt% of the solids collected
312 at the end of the experiment. The XRD diffractograms of the solids collected after the experiments
313 are nearly identical to those of the pre-experiment solids, other than a small increase in the 20-40 2θ

range (Figure 4C). This could indicate the presence of a minor quantity of an amorphous phase. No evidence for the precipitation of an amorphous phase, however, could be found in the SEM images (Figure 4A-B).

4.3. Sepiolite dissolution experiments

The temporal evolution of the aqueous Mg^{2+} and Si concentrations during the dissolution experiments shows an initial rapid increase in the Mg^{2+} and Si concentrations. These concentrations subsequently decrease slightly as the system attains steady-state and the concentrations remain constant over time (Fig. 5). An initial rapid aqueous Si and Mg^{2+} release at the onset of Mg-silicate mineral dissolution experiments has been previously reported by cf. Luce et al. (1972), Mulders and Oelkers (2020) and Oelkers and Schott (2001). This behaviour has been attributed to the relatively rapid release of partially detached Si and Mg^{2+} on the mineral surface and attributed to sample preparation. During these sepiolite dissolution experiments up to 16 mg of the initial ~300 mg of sepiolite dissolved.

In the dissolution experiments, the aqueous Si/Mg ratio at the onset of the experiments is lower than the Si/Mg ratio of the crystalline sepiolite, suggesting the preferential release of Mg from the solid. This is consistent with the results reported by Mulders et al. (2018) and Mulders and Oelkers (2020). These previous studies attributed the initial non-stoichiometric release of Si and Mg^{2+} at near-neutral pH conditions to the dissolution mechanism of sepiolite. At these pH conditions, sepiolite dissolves via the initial exchange of Mg^{2+}, followed by the relative slow breaking of the Si tetrahedra. The preferential initial release of Mg from the minerals enstatite, olivine, and diopside at similar pH and temperature conditions during surface titration experiments were reported and interpreted in detail by Oelkers et al. (2009).

4.4. Sepiolite growth and dissolution rates as a function of chemical affinity

Sepiolite growth and dissolution rates were computed using Eq. 8 and are reported in Table 2. To exclude the effect of potential brucite precipitation on the computed growth rates, only rates calculated from the changes in reactive aqueous solution Si concentrations are considered. Computed sepiolite precipitation rates are in the same range as those reported by Arizaleta et al. (2020). The uncertainty associated with the computed rates is ~15% as computed via error propagation and stems from uncertainties in the Si and Mg concentrations (~2.5% or less), the uncertainties in the measured pH (±0.04 pH), the uncertainty in the measured fluid flow rate (~4%) and the uncertainties of the measured surface area (±10%).

To assess whether sepiolite dissolution and growth mechanisms are consistent with TST and can thus be described using Eq. 5, the Si release and consumption rates are plotted versus $\exp\left(\frac{\Delta G_r}{\sigma RT}\right) - 1$ using the equilibrium constants provided by Christ et al. (1973) (K_{sp} = $10^{27.66}$) and by Wolery and Jove-Colon (2004) (K_{sp} = $10^{27.17}$) in Fig. 6. Temkin's number, equal to the ratio of the rate of destruction of the activated or precursor complex relative to the overall rate, is assumed to be 6 consistent with the number of Si atoms in one mole of sepiolite. The surface area normalized dissolution and growth rates can then be fitted using a least square linear fit. These fits provides the following rate equations:

$$r = -10^{-14.02} * \left(1 - \exp\left(\frac{\Delta G_r}{6RT}\right)\right) - 8.60 * 10^{-18}, \text{ when } K_{sp} = 10^{27.17} \quad (10)$$

and

$$r = -10^{-14.02} * \left(1 - \exp\left(\frac{\Delta G_r}{6RT}\right)\right) - 6.82 * 10^{-18}, \text{ when } K_{sp} = 10^{27.66} \quad (11)$$

The coefficient of determination, R^2, of both these fits 0.947, suggesting a good description of the measured rates using either K_{sp} = $10^{27.17}$ and K_{sp} = $10^{27.66}$ respectively. In both rate equations $-10^{-14.02}$ represents the forward rate of the reaction (r_+) in mol/cm^2/s.

5. Discussion

5.1. Thermodynamic equilibrium constant of the sepiolite hydrolysis reaction

Although the quality of the linear fits of the measured rates in Figure 6 are both high as indicated by the R^2 of the two regression equations (Eq. 10 and 11), these fits do not intercept the origin. This suggests that the equilibrium constants used in these regressions are somewhat inconsistent with the experimental observations. Assuming that the reaction rate is 0 at equilibrium and that the reaction mechanism does not change as a function of chemical affinity, an equilibrium constant consistent with our experiments can be derived by fitting the data using a least square linear fit and the requirement that rates equal zero at equilibrium (Saldi et al., 2012). Figure 7 provides the results of this fit. When K_{sp} is assumed to be $10^{29.25\pm1.70}$ the R^2 of the regression equation equals 0.948 and the resulting rate equation intercepts the origin. Although the retrieved equilibrium constant is slightly higher than corresponding values reported by Christ et al. (1973) (K_{sp} = $10^{27.66}$) and by Wolery and Jove-Colon (2004) (K_{sp} = $10^{27.17}$), these past constants are almost within the uncertainty as the value generated by the regression of rates measured in the present study. The regression line in Fig. 7 is consistent with:

$$r = -10^{-14.80} * \left(1 - \exp\left(\frac{\Delta G_r}{6RT}\right)\right) \quad (12)$$

where $-10^{-14.80}$ reflects the surface area normalized forward rate of the reaction in mol/cm^2/s.

Differences in measured equilibrium constants for mineral hydrolysis constants are not uncommon and can be attributed to small changes in the crystal structure, chemical composition and/or to differences in the experimental approach (Bénézeth et al., 2018). Note the Mg to Si ratio of the sepiolite used in our experiments, differs somewhat from that used in some of the previous experiments used to deduce the equilibrium constant of its hydrolysis reaction. Further differences between the reported equilibrium constants can stem from the uncertainties associated with the pH

385 and aqueous Mg^{2+} and Si measurements, and the calculation of activity coefficients of the aqueous
386 species. A slightly higher equilibrium constant of synthetic sepiolite was reported by Baldermann et
387 al. (2018) and attributed to the relatively lower crystallinity of the precipitated phase and a
388 difference in chemical composition of the synthetic phase compared to natural sepiolite.

389

390 ***5.2. The mechanism of sepiolite dissolution and growth***

391 The linear dependence between the sepiolite dissolution and growth rates, and $1 - \exp\left(\frac{\Delta G_r}{\sigma RT}\right)$
392 (Eq. 12) suggests that these rates are consistent with Eq. 5 and thus with TST together with the law
393 of detailed balancing. According to Nagy et al. (1991) Eq. 5 only holds when growth and dissolution
394 are controlled by the same elementary reaction step, when the magnitude of ΔG_r is not significantly
395 greater than *RT,* and when the number of reactive surface sites remains constant over time. Based
396 on observations of sepiolite dissolution rates as a function of aqueous solution pH at far from
397 equilibrium, Mulders and Oelkers (2020) concluded that at circum-neutral pH sepiolite dissolution
398 rates are limited by the hydration of the silanol groups. The linearity of the rate-law such as shown in
399 Figs 6 and 7, therefore suggests that the dehydration of the silanol groups ($Si(OH)_4$) is the rate
400 limiting step during sepiolite growth during the experiments of this study.

401 Previous work on kaolinite precipitation provides further evidence for the dehydration of silanol
402 groups as the rate-limiting step for clay mineral growth. Devidal et al. (1997) concluded that the rate
403 of kaolinite growth at pH 2 and 150 ^{o}C is limited by the dehydration of silanol groups. As kaolinite is
404 an Al-rich phyllosilicate, its growth mechanism might differ from that of the Mg-rich sepiolite.
405 Nevertheless, it seems reasonable to a first approximation that these results could be extrapolated
406 to sepiolite and clays in general. As breaking bonds is generally slower than making bonds, the rate
407 of clay mineral growth is likely limited by either the rate of dehydration of either aqueous Mg or Al,
408 or of aqueous silica. Although clay minerals have a relatively high water content, the dehydration of
409 aqueous metals including Si is necessary to form its crystal structure. Helm and Merbach (1999)

showed that the rate of aqueous Al dehydration is slower than the rate of Mg dehydration. Hence, if the rate of aqueous Si dehydration limits the rate of kaolinite precipitation, despite the relatively slow dehydration rate of Al, aqueous Si dehydration will likely also limit the rate of sepiolite growth and thus the rate of clay mineral growth in general.

This conclusion contrasts to that from that of Brady (1992) and of Baldermann et al. (2018). Brady (1992), based on the variation of surface normalized dissolution rates as a function of pH argued that at pH<9, the dehydration of aqueous Mg^{2+} is the rate limiting step of sepiolite precipitation. Icopini et al. (2005) showed that at circum-neutral pH the oligomerization of silica increases, and silica structures become more stable. Based on these arguments, Baldermann et al. (2018) hypothesized that at circum-neutral pH, sepiolite precipitation is limited by Mg dehydration. To explore this possibility Baldermann et al. (2018) performed batch sepiolite growth experiments in initial aqueous solutions that were strongly supersaturated with respect to sepiolite. In these experiments the precipitation of sepiolite proceeded via the initial nucleation of a sepiolite-like polysome, followed by its recrystallization to a more crystalline sepiolite-like phase. This mechanism, however, likely differs from that of sepiolite growth at the closer to equilibrium conditions of our experiments. The close correspondence between measured dissolution and precipitation rates in our experiments suggests the dominant sepiolite precipitation mechanism is the attachment of metals to existing reactive sites rather than the nucleation of new sites or amorphous precursors. The contrasting precipitation behaviours in our near to equilibrium experiments compared to the far from equilibrium experiments reported by Baldermann et al. (2018) likely stems from distinct precipitation mechanism dominating in the different experiments.

Many previous studies of sepiolite and smectite precipitation do not distinguish between nucleation and growth mechanisms (Linares and Huertas, 1971; Tutolo and Tosca, 2018; Wollast et al., 1968; Zhang et al., 2010). Typically, these studies consider precipitation in non-seeded experiments from initially highly supersaturated aqueous solutions in batch experiments. The initial

precipitated phase in such experiments is poorly crystalline and hydrous; this initial solid is thought to dehydrate and recrystallize over time. Similarly, previous work on smectite synthesis suggests that clay mineral precipitation in batch reactors from initially highly supersaturated aqueous solutions proceeds via the initial precipitation of a gibbsite or brucite-like phase, followed by the partial dehydration of these phases and the sorption of Si (Linares and Huertas, 1971; Zhang et al., 2010). Such experiments differ fundamentally from those of the present study. In highly supersaturated solutions, the precipitation of a solid from the aqueous solution can proceed via the spontaneous nucleation of an amorphous phase, followed by absorption of a (hydrated) aqueous species to the nuclei and the clustering of the precipitated nuclei (Baldermann et al., 2018; Guggenheim and Krekeler, 2011; Hindshaw et al., 2019; Tosca and Masterson, 2014). In contrast, the growth of crystalline minerals at closer to equilibrium conditions, such as the experiments performed in the present study proceeds via the continuous attachment of dehydrated reactants to reactive surface sites (Benning and Waychunas, 2008; Schott et al., 2012, 2009). Differences in the mechanisms between nucleation and crystalline growth likely account for the observed differences in the rate limiting step between sepiolite synthesis at far from equilibrium and sepiolite growth at closer to equilibrium conditions.

Although the results of the shorter-term growth experiments and dissolution experiments in this study are consistent with Eq. 12 and can thus be interpreted within the framework of TST, the longer term experiments show a decrease in the growth rate, suggesting a loss of reactive sites over time (Figure 3). Schott et al. (2012) hypothesized that the morphology of the mineral can be linked to the mineral growth mechanism and thus to the nature of the rate equation. Transition state theory based rate equations have been successfully applied to describe the precipitation rates of metal-oxides, hydroxycarbonates and some clays (Bénézeth et al., 2008; Pokrovsky and Schott, 2004; Yang and Steefel, 2008). Such metal-oxides, salts and hydroxycarbonates have relatively large reactive surface areas and the number of reactive sites during the growth of these minerals remains close to constant as the mineral grows. In contrast, reactive surface sites on many more crystalline or

461 anhydrous minerals appear to be more rapidly destroyed over time as these minerals grow and form
462 more ideal crystal forms. The destruction of reactive surface sites during sepiolite growth is
463 evidenced by the decrease in precipitation rates during the longer-term growth experiment.
464 Previous work on the precipitation rates of kaolinite equally observed that the rates of precipitation
465 slowed over time (Yang and Steefel, 2008). The authors argued that such a change in the growth
466 mechanism is related to the availability of reactive surface area on the seed material. Over time
467 growth slows as reactive sites are destroyed and the heterogenous nucleation of new reactive
468 surface sites on the mineral surface is required for further growth. Similarly, Gautier (1999) and Saldi
469 et al. (2009) showed that the growth mechanism of quartz and magnesite depends on the number of
470 available reactive surface sites. Growth rates measured on pre-dissolved quartz particles, a process
471 creating an equal number of either dissolution or precipitation reactive sites were found to be
472 consistent with TST and the corresponding quartz dissolution rates, whilst the growth of quartz
473 grains that were not pre-dissolved was far slower (Gautier, 1999).

474 Further evidence that reactive surface sites can be destroyed during mineral growth is provided
475 by experiments on dolomite growth using hydrothermal atomic force microscopy (Berninger et al.,
476 2017). Studies of the growth kinetics and mechanisms of dolomite showed that the long-term
477 dolomite growth is hindered by the precipitation of a non-stoichiometric, non-ordered monolayer on
478 the initially pristine surface. This first layer closely mimics the surface morphology of dolomite. The
479 precipitation of this layer, however, poisons reactive surface sites and thereafter dolomite growth is
480 only observed via the nucleation of 2-islands on the surface (Berninger et al., 2017).

481

482 ***5.3. Controls on weathering rates***

483 Several authors have suggested that the sluggish growth of clay minerals controls weathering
484 rates in natural environments (Maher et al., 2009; Zhu and Lu, 2009). Weathering involves the
485 dissolution of primary minerals coupled to the precipitation of secondary products. The potential to

dissolve primary minerals depends on the ion activation product of its dissolution products in the reactive aqueous solution, which, in turn, depends on how fast secondary minerals precipitate. Zhu and Lu (2009) showed that in batch dissolution experiments containing feldspar and the secondary minerals, including kaolinite, the aqueous fluids were strongly supersaturated with respect to the secondary clay minerals. The authors concluded that when the ratio of the effective rate constants between the secondary phase and feldspar ranged between 10^{-2} and 10^{-4}, slow clay mineral growth became the rate limiting step of the overall coupled dissolution/precipitation process (Zhu et al., 2004a, 2004b).

This conclusion can be tested by taking account of the results of this study and calculating the rates of enstatite or forsterite dissolution and coupled to the rates of sepiolite growth as a function of mineral surface area. Such coupled reactions have, for example, been observed in ultramafic-rock-hosted veins in Turkey (Yalcin and Bozkaya, 2004). For these calculations it is assumed that the fluid compositions of the system are at steady-state, whereby the aqueous Mg^{2+} and Si concentrations and the pH do not change over time. The dissolution reactions of forsterite and enstatite are respectively:

$$\mathrm{Mg_2SiO_4 + 4H^+ \leftrightarrow SiO_2 + 2H_2O + 2Mg^{2+}} \quad (13)$$

$$\mathrm{MgSiO_3 + 2H^+ \leftrightarrow H_2O + Mg^{2+} + SiO_2} \quad (14)$$

The surface area normalized rates of forsterite and enstatite dissolution can be calculated from (Rimstidt et al., 2012; Oelkers and Schott, 2001):

$$r_+ = k_+ * \left(1 - \frac{IAP}{K}\right) \quad (15)$$

where the IAP is the ion activation product of the dissolving mineral, and K represents the equilibrium constant of the dissolution reactions (13) or (14). The rate constant of the dissolution reaction (k_+) at pH = 8 at 60 °C is taken as 1.58 x 10^{-13} mol/cm^2/s for forsterite (Rimstidt et al., 2012) and 9.23 x 10^{-13} mol/cm^2/s for enstatite (Oelkers and Schott, 2001). At 60 °C, the equilibrium

constants of forsterite and enstatite are respectively $10^{24.01}$ and $10^{9.73}$ (Johnson et al., 1992). The aqueous Si concentrations in the calculations were assumed to be constant and in equilibrium with amorphous silica (SiO_2(am)). The pH was held constant at 8 to mimic the pH conditions of the experiments performed in this study.

The coupled dissolution and precipitation rates are then computed noting that at steady state:

$$SSA_{Fo/En}\, r_{Fo/En} = -\frac{\nu_{Mg,\frac{Fo}{En}}}{\nu_{Mg,Sep}} SSA_{Sep}\, r_{Sep} \quad (16)$$

where $\nu_{Mg,Fo/En}$ and $\nu_{Mg,Sep}$ refer to the number of moles of Mg in one mole of forsterite or enstatite and sepiolite, and $SSA_{Fo/En}$ and SSA_{Sep} represent the BET specific surface area of these minerals respectively. Therefore, at steady-state

$$k_{Fo/En} * SSA_{Fo/En} * \left(1 - \frac{IAP_{Fo/En}}{K_{Fo/En}}\right) = -k_{sep} * SSA_{Sep} * \frac{\nu_{Mg,Fo/En}}{\nu_{Mg,Sep}} * \left(1 - \left(\frac{IAP_{Sep}}{K_{Sep}}\right)^{1/\sigma}\right) \quad (17)$$

where again the subscript Fo/En denotes either forsterite or enstatite and the subscript Sep refers to sepiolite. Equations (16) and (17) were solved by fixing the ratio of the mineral surface areas ($SSA_{Sep}/SSA_{Fo/En}$) to acquire the aqueous Mg concentration of the reactive fluid. This Mg concentration was then used to determine the *IAP* and thus the reaction rates of each solid from Equations (12) and (15).

Figure 8 shows the results of these calculations. The rate of forsterite and enstatite dissolution increase when surface area ratio ($SSA_{Sep}/SSA_{Fo/En}$) increases. The rate of forsterite dissolution becomes independent of sepiolite surface area, and equal to the far from equilibrium forsterite dissolution rates when the sepiolite/forsterite surface area ratio exceeds 10. Thus, only when the surface area of forsterite is more than 10 times lower than that of sepiolite, forsterite dissolution is influenced by the precipitation rates of sepiolite. Equally, only when the surface area of enstatite is

more than 100 times lower than the surface area sepiolite, enstatite dissolution is influenced by the precipitation rate of sepiolite.

The saturation indexes of forsterite/enstatite and sepiolite, determine the degree to which forsterite/enstatite dissolution or sepiolite growth controls their coupled reaction. At low $SSA_{Sep}/SSA_{Fo/En}$ the saturation index of sepiolite is high, and forsterite/enstatite are close to equilibrium to the fluid phase. In this case the overall reaction rates slow as the dissolution rates of the primary phases decreases as equilibrium is approached. Under such conditions the overall reaction rate is limited by the slow growth rates of the clay minerals. In contrast, at higher. $SSA_{Sep}/SSA_{Fo/En}$ sepiolite is close to equilibrium and forsterite/enstatite are strongly undersaturated. Under such conditions the overall coupled rates are equal to the far from equilibrium dissolution rates of the primary phases. At such conditions, the clay grows sufficiently fast to rapidly consume the Mg^{2+} and Si liberated from the dissolving primary minerals. Under such conditions, the overall rate is considered to be limited by the dissolution rate of the primary mineral. The surface area of clay minerals in natural systems are typically several orders of magnitude larger than that of primary silicates. As such the calculations above suggest that in most systems the rate of forsterite and enstatite dissolution in weathering systems would be limited by the dissolution rates of these primary minerals.

To explore the degree to which either forsterite/enstatite dissolution or sepiolite growth limits weathering rates in natural systems, the solution saturation states of clays and primary mineral in Icelandic waters were computed using PHREEQC together with its llnl database. The solution compositions of these waters were taken from Arnórsson et al. (1983), Gislason (1989), Gislason and Arnórsson (1993), Stefánsson et al. (2001) and Stefánsson and Gislason (2001). The temperature and pH of these geothermal and surface waters ranged between 1-100 °C and 5-11 respectively. Primary rocks in Iceland are relatively rich in forsterite and enstatite and the waters of Iceland thus provide a natural analogue for the system modelled in Figure 8. Figure 9 shows the computed saturation

557 states of forsterite, enstatite, diopside, kaolinite, sepiolite and montmorillonite in the Icelandic
558 waters as a function of the pH. When the pH of the solution is ≥8, the solution is in approximately
559 equilibrium with the enstatite and forsterite, while the aqueous fluid is strongly supersaturated with
560 respect to sepiolite. Despite this, sepiolite is rarely, if ever, found as an alteration product in these
561 systems. Note that the sepiolite solution saturation state in these natural waters is similar to those
562 considered in the sepiolite growth experiments performed in this study.

563 The results of the computed mineral saturation states in the natural waters apparently disagree
564 with the results of the computations in Figure 8. Calculations performed using laboratory measured
565 sepiolite growth rates obtained from the shorter-term experiments suggest that the coupled rates of
566 sepiolite growth and forsterite or enstatite dissolution are likely limited by the slow dissolution rates
567 of the primary minerals and the coexisting aqueous phase will be close to equilibrium with respect
568 to sepiolite, but strongly undersaturated with respect to forsterite and enstatite. This discrepancy
569 suggests that sepiolite precipitation rates are inconsistent with Eq. 12 in natural systems. It seems
570 likely that in natural systems, as suggested by slowing of rates observed in the longer-term
571 experiments of this study, reactive sites on the clay mineral surface become scarce and new reactive
572 sites must be nucleated on the clay mineral surfaces to continue clay mineral growth. In such cases
573 the nucleation of new reactive sites on the sepiolite surface rather that the growth of sepiolite on
574 existing reactive sites will become rate limiting.

575 Notably, gibbsite, brucite and SiO_2(am) are close to equilibrium with the solution in the Icelandic
576 waters (Fig. 9). Stefánsson et al. (2001) further showed that the Icelandic waters were in equilibrium
577 with respect to ferrihydrites, goethite and hematite. These observations suggest that under natural
578 conditions, the rate of metal-oxide and SiO_2(am) precipitation is fast compared to the precipitation
579 of clays (Arizaleta et al., 2020; Bénézeth et al., 2008; Fraysse et al., 2006; Pokrovsky and Schott,
580 2004; Yang and Steefel, 2008).

581 The precipitation of sepiolite in natural systems is further affected by the consumption of Mg and
582 Si by organisms and by abiotic reactions. For example, silicifying organisms control the Si
583 concentrations in the oceans, while Mg concentrations are affected by carbonate mineral
584 precipitation (Tipper et al., 2006; Treguer et al., 1995). In many systems the Si and Mg
585 concentrations therefore remain low, hindering the precipitation of sepiolite. Equally, the relatively
586 low pH of many natural waters limits the precipitation of sepiolite in such systems. Biomineralization
587 and the competition with other clay minerals could further hinder the precipitation of sepiolite in
588 natural systems (Tutolo and Tosca, 2018).

589

590 6. Summary and concluding remarks

591 Sepiolite growth and dissolution rates in shorter-term flow through experiments are found to be
592 consistent with Transition State Theory based rate equations. Such a relationship implicates an
593 identical number of reactive surface sites on the clay mineral surface during dissolution and growth.
594 However, in the longer-term flow through experiments, the rate of sepiolite growth decreased over
595 time. Such a decrease could be associated with the destruction of sepiolite reactive surface sites
596 over time as the mineral grew.

597 Geochemical calculations based on the shorter-term sepiolite growth rates suggest that clay
598 mineral precipitation rates should be rapid compared to the dissolution of primary minerals in
599 natural systems, yet field evidence shows this to be incorrect. It seems likely that over the long-term,
600 reactive sites at the sepiolite mineral surface are destroyed by the growth process and the long-term
601 precipitation of sepiolite is limited by the relatively slow nucleation of new reactive surface sites on
602 its surfaces. Such observations call for the development of new robust rate models for the more
603 accurate description of mineral precipitation in natural systems.

References

Arizaleta, M.L., Nightingale, M., Tutolo, B.M., 2020. A rate law for sepiolite growth at ambient temperatures and its implications for early lacustrine diagenesis. Geochim. Cosmochim. Acta 288, 301–315. https://doi.org/https://doi.org/10.1016/j.gca.2020.08.014

Arnorsson, S., Gunnlaugsson, E., Svavarsson, H., 1983. The chemistry of geothermal waters in Iceland. II. Mineral equilibria and independent variables controlling water compositions. Geochim. Cosmochim. Acta 47, 547–566.

Arvidson, R.S., Luttge, A., 2010. Mineral dissolution kinetics as a function of distance from equilibrium - New experimental results. Chem. Geol. 269, 79–88. https://doi.org/10.1016/j.chemgeo.2009.06.009

Avnimelech, Y., McHenry, J.R., 1984. Enrichment of transported sediments with organic carbon, nutrients, and clay. Soil Sci. Soc. Am. J. 48, 259–266.

Baldermann, A., Mavromatis, V., Frick, P.M., Dietzel, M., 2018. Effect of aqueous Si/Mg ratio and pH on the nucleation and growth of sepiolite at 25 °C. Geochim. Cosmochim. Acta 227, 211–226. https://doi.org/10.1016/j.gca.2018.02.027

Beig, M.S., Lüttge, A., 2006. Albite dissolution kinetics as a function of distance from equilibrium: Implications for natural feldspar weathering. Geochim. Cosmochim. Acta 70, 1402–1420. https://doi.org/10.1016/j.gca.2005.10.035

Bénézeth, P., Berninger, U.-N., Bovet, N., Schott, J., Oelkers, E.H., 2018. Experimental determination of the solubility product of dolomite at 50-253 C. Geochim. Cosmochim. Acta 224, 262–275.

Bénézeth, P., Palmer, D.A., Wesolowski, D.J., 2008. Dissolution/precipitation kinetics of boehmite and gibbsite: Application of a pH-relaxation technique to study near-equilibrium rates. Geochim. Cosmochim. Acta 72, 2429–2453. https://doi.org/10.1016/J.GCA.2008.02.019

Benning, L.G., Waychunas, G.A., 2008. Nucleation, Growth, and Aggregation of Mineral Phases: Mechanisms and Kinetic Controls. Kinet. Water-Rock Interact. 259–333. https://doi.org/10.1007/978-0-387-73563-4_7

Berner, R.A., 1992. Weathering, plants, and the long-term carbon cycle. Geochim. Cosmochim. Acta 56, 3225–3231.

Berner, R.A., 1964. Stability fields of iron minerals in anaerobic marine sediments. J. Geol. 72, 826–834.

Berninger, U.-N., Saldi, G.D., Jordan, G., Schott, J., Oelkers, E.H., 2017. Assessing dolomite surface reactivity at temperatures from 40 to 120 C by hydrothermal atomic force microscopy. Geochim. Cosmochim. Acta 199, 130–142.

Bowles, F.A., Angino, E.A., Hosterman, J.W., Galle, O.K., 1971. Precipitation of deep-sea palygorskite and sepiolite. Earth Planet. Sci. Lett. 11, 324–332. https://doi.org/10.1016/0012-821X(71)90187-7

Brady, P. V, 1992. Surface complexation and mineral growth: Sepiolite, in: International Symposium on Water-Rock Interaction. pp. 85–88.

Brantley, S.L., 2008. Kinetics of mineral dissolution, in: Kinetics of Water-Rock Interaction. Springer, pp. 151–210.

Brunauer, S., Emmett, P.H., Teller, E., 1938. Adsorption of gases in multimolecular layers. J. Am. Chem. Soc. 60, 309–319.

Burch, T.E., Nagy, K.L., Lasaga, A.C., 1993. Free energy dependence of albite dissolution kinetics at

80°C and pH 8.8. Chem. Geol. 105, 137–162. https://doi.org/10.1016/0009-2541(93)90123-Z

Burton, W.K., Cabrera, N., Frank, F.C., 1951. The Growth of Crystals and the Equilibrium Structure of their Surfaces. Philos. Trans. R. Soc. A Math. Phys. Eng. Sci. 243, 299–358. https://doi.org/10.1098/rsta.1951.0006

Chamley, H., 2013. Clay sedimentology. Springer Science & Business Media.

Christ, C.L., Hostetler, P.B., Siebert, R.M., 1973. Studies in the system MgO-SiO_2-CO_2-H_2O (III); the activity-product constant of sepiolite.pdf. Am. J. Sci. 273, 65–68.

De Yoreo, J.J., Vekilov, P.G., 2003. Principles of crystal nucleation and growth. Rev. Mineral. geochemistry 54, 57–93.

Devidal, J.-L., Schott, J., Dandurand, J.-L., 1997. An experimental study of kaolinite dissolution and precipitation kinetics as a function of chemical affinity and solution composition at 150°C, 40 bars, and pH 2, 6.8, and 7.8. Geochim. Cosmochim. Acta 61, 5165–5186. https://doi.org/10.1016/S0016-7037(97)00352-9

Eyring, H., 1938. The theory of absolute reaction rates. Trans. Faraday Soc. 34, 41–48.

Fraysse, F., Pokrovsky, O.S., Schott, J., Meunier, J.-D., 2006. Surface properties, solubility and dissolution kinetics of bamboo phytoliths. Geochim. Cosmochim. Acta 70, 1939–1951.

Gautier, J.-M., 1999. Etude expérimentale et modélisation de la cinétique de dissolution et de cristallisation des silicates en milieu hydrothermal: cas du quartz et du feldspath potassique. Toulouse 3.

Gislason, S.R., 1989. Kinetics of water-air interactions in rivers: a field study in Iceland, in: International Symposium on Water-Rock Interaction. 6. pp. 263–266.

Gislason, S.R., Arnórsson, S., 1993. Dissolution of primary basaltic minerals in natural waters: saturation state and kinetics. Chem. Geol. 105, 117–135.

Gislason, S.R., Wolff-Boenisch, D., Stefansson, A., Oelkers, E.H., Gunnlaugsson, E., Sigurdardottir, H., Sigfusson, B., Broecker, W.S., Matter, J.M., Stute, M., Axelsson, G., Fridriksson, T., 2010. Mineral sequestration of carbon dioxide in basalt: A pre-injection overview of the CarbFix project. Int. J. Greenh. Gas Control 4, 537–545. https://doi.org/10.1016/J.IJGGC.2009.11.013

Guggenheim, S., Krekeler, M.P.S., 2011. The Structures and Microtextures of the Palygorskite–Sepiolite Group Minerals. Dev. Clay Sci. 3, 3–32. https://doi.org/10.1016/B978-0-444-53607-5.00001-3

Harrison, A.L., Power, I.M., Dipple, G.M., 2012. Accelerated carbonation of brucite in mine tailings for carbon sequestration. Environ. Sci. Technol. 47, 126–134.

Helgeson, H., Delany, J., Nesbitt, H., Bird, D.K., 1978. Summary and critique of the thermodynamic properties of rock-forming minerals. Am. J. Sci. 278A, 1–129.

Helgeson, H.C., Kirkham, D.H., 1976. Theoretical prediction of thermodynamic properties of aqueous electrolytes at high pressures and temperatures. III. Equation of state for aqueous species at infinite dilution. Am. J. Sci.;(United States) 276.

Hellmann, R., Tisserand, D., 2006. Dissolution kinetics as a function of the Gibbs free energy of reaction: An experimental study based on albite feldspar. Geochim. Cosmochim. Acta 70, 364–383.

Helm, L., Merbach, A.E., 1999. Water exchange on metal ions: experiments and simulations. Coord. Chem. Rev. 187, 151–181.

Hem, J.D., Lind, C.J., 1974. Kaolinite synthesis at 25 °C. Science (80-.). 184, 1171–1173.

690 Hendricks, S.B., Fry, W.H., 1930. The results of X-ray and microscopical examinations of soil colloids.
691 Soil Sci. 29, 457–480.

692 Hindshaw, R.S., Tosca, R., Goût, T.L., Farnan, I., Tosca, N.J., Tipper, E.T., 2019. Experimental
693 constraints on Li isotope fractionation during clay formation. Geochim. Cosmochim. Acta 250,
694 219–237. https://doi.org/10.1016/J.GCA.2019.02.015

695 Icopini, G.A., Brantley, S.L., Heaney, P.J., 2005. Kinetics of silica oligomerization and nanocolloid
696 formation as a function of pH and ionic strength at 25 C. Geochim. Cosmochim. Acta 69, 293–
697 303.

698 Jiang, C.Z., Tosca, N.J., 2020. Growth kinetics of siderite at 298.15 K and 1 bar. Geochim. Cosmochim.
699 Acta 274, 97–117.

700 Katsumi, T., Invui, T., Kamon, M., 2010. In-situ containment for waste landfill and contaminated
701 sites, in: Advances in Environmental Geotechnics. Springer, pp. 248–258.

702 Kent, D.B., Kastner, M., 1985. Mg^{2+} removal in the system Mg^{2+}—amorphous SiO_2—H_2O by
703 adsorption and Mg-hydroxysilicate precipitation. Geochim. Cosmochim. Acta 49, 1123–1136.
704 https://doi.org/10.1016/0016-7037(85)90003-1

705 Lasaga, A.C., 1995. Fundamental approaches in describing mineral dissolution and precipitation
706 rates. Chem. Weather. rates Silic. Miner. 23–86.

707 Linares, J., Huertas, F., 1971. Kaolinite: Synthesis at Room Temperature. Science (80-.). 171, 896–
708 897. https://doi.org/10.1126/science.171.3974.896

709 Luce, R.W., Bartlett, R.W., Parks, G.A., 1972. Dissolution kinetics of magnesium silicates. Geochim.
710 Cosmochim. Acta 36, 35–50. https://doi.org/10.1016/0016-7037(72)90119-6

711 Maher, K., Steefel, C.I., White, A.F., Stonestrom, D.A., 2009. The role of reaction affinity and
712 secondary minerals in regulating chemical weathering rates at the Santa Cruz Soil
713 Chronosequence, California. Geochim. Cosmochim. Acta 73, 2804–2831.

714 Malusis, M.A., Shackelford, C.D., Olsen, H.W., 2003. Flow and transport through clay membrane
715 barriers. Eng. Geol. 70, 235–248.

716 Misaelides, P., 2019. Clay minerals and zeolites for radioactive waste immobilization and
717 containment: a concise verview, in: Modified Clay and Zeolite Nanocomposite Materials.
718 Elsevier, pp. 243–274.

719 Mulders, J.J.P.A., Harrison, A.L., Christ, J., Oelkers, E.H., 2018. Non-stoichiometric dissolution of
720 sepiolite. Energy Procedia 146, 74–80.

721 Mulders, J.J.P.A., Oelkers, E.H., 2020. An experimental study of sepiolite dissolution rates and
722 mechanisms at 25° C. Geochim. Cosmochim. Acta 270, 296–312.

723 Nagy, K.L., Blum, A.E., Lasaga, A.C., 1991. Dissolution and Precipitation kinetics of kaolinite at 80℃
724 and pH3: the dependence on solution saturation state. Am. J. Sci. 291, 649–686.

725 Nagy, K.L., Lasaga, A.C., 1992. Dissolution and precipitation kinetics of gibbsite at 80°C and pH 3: The
726 dependence on solution saturation state. Geochim. Cosmochim. Acta 56, 3093–3111.
727 https://doi.org/10.1016/0016-7037(92)90291-P

728 Oelkers, E.H., 2001. An experimental study of forsterite dissolution rates as a function of
729 temperature and aqueous Mg and Si concentrations. Chem. Geol. 175, 485–494.
730 https://doi.org/10.1016/S0009-2541(00)00352-1

731 Oelkers, E.H., Schott, J., 2001. An experimental study of enstatite dissolution rates as a function of
732 pH, temperature, and aqueous Mg and Si concentration, and the mechanism of
733 pyroxene/pyroxenoid dissolution. Geochim. Cosmochim. Acta 65, 1219–1231.

734 Oelkers, E.H., Schott, J., 1995. Experimental study of anorthite dissolution and the relative
735 mechanism of feldspar hydrolysis. Geochim. Cosmochim. Acta 59, 5039–5053.

736 Oelkers, E.H., Schott, J., Devidal, J.-L., 2001. On the interpretation of closed system mineral
737 dissolution experiments: comment on''Mechanism of kaolinite dissolution at room
738 temperature and pressure part II: kinetic study''by Huertas et al.(1999). GeCoA 65, 4429–4432.

739 Oelkers, E.H., Schott, J., Devidal, J.L., 1994. The effect of aluminum, pH, and chemical affinity on the
740 rates of aluminosilicate dissolution reactions. Geochim. Cosmochim. Acta 58, 2011–2024.
741 https://doi.org/10.1016/0016-7037(94)90281-X

742 Pauling, L., 1930. The structure of the micas and related minerals. Proc. Natl. Acad. Sci. U. S. A. 16,
743 123.

744 Perraki, T., Orfanoudaki, A., 2008. Study of raw and thermally treated sepiolite from the Mantoudi
745 area, Euboea, Greece: X-ray diffraction, TG/DTG/DTA and FTIR investigations. J. Therm. Anal.
746 Calorim. 91, 589–593.

747 Pokrovsky, O.S., Schott, J., 2004. Experimental study of brucite dissolution and precipitation in
748 aqueous solutions: surface speciation and chemical affinity control. Geochim. Cosmochim. Acta
749 68, 31–45. https://doi.org/10.1016/S0016-7037(03)00238-2

750 Rimstidt, J.D., Brantley, S.L., Olsen, A.A., 2012. Systematic review of forsterite dissolution rate data.
751 Geochim. Cosmochim. Acta 99, 159–178.

752 Saldi, G.D., Jordan, G., Schott, J., Oelkers, E.H., 2009. Magnesite growth rates as a function of
753 temperature and saturation state. Geochim. Cosmochim. Acta 73, 5646–5657.
754 https://doi.org/10.1016/J.GCA.2009.06.035

755 Saldi, G.D., Schott, J., Pokrovsky, O.S., Gautier, Q., Oelkers, E.H., 2012. An experimental study of
756 magnesite precipitation rates at neutral to alkaline conditions and 100-200 °C as a function of
757 pH, aqueous solution composition and chemical affinity. Geochim. Cosmochim. Acta 83, 93–
758 109.

759 Schott, J., Oelkers, E.H., Bénézeth, P., Goddéris, Y., François, L., 2012. Can accurate kinetic laws be
760 created to describe chemical weathering? Comptes Rendus Geosci. 344, 568–585.

761 Schott, J., Pokrovsky, O.S., Oelkers, E.H., 2009. The Link Between Mineral Dissolution/Precipitation
762 Kinetics and Solution Chemistry. Rev. Mineral. Geochemistry 70, 207–258.
763 https://doi.org/10.2138/rmg.2009.70.6

764 Shafizadeh, A., Gimmi, T., Van Loon, L.R., Kaestner, A.P., Mäder, U.K., Churakov, S. V, 2020. Time-
765 resolved porosity changes at cement-clay interfaces derived from neutron imaging. Cem.
766 Concr. Res. 127, 105924.

767 Shao, H., Ray, J.R., Jun, Y.-S., 2010. Dissolution and precipitation of clay minerals under geologic CO2
768 sequestration conditions: CO2- brine- phlogopite interactions. Environ. Sci. Technol. 44, 5999–
769 6005.

770 Stefansson, A., Gislason, S.R., 2001. Chemical weathering of basalts, SW Iceland. Effect of rock
771 crystallinity, weathering minerals and vegetative cover on chemical fluxes to the ocean. Am. J.
772 Sci 301, 513–556.

773 Stefansson, A., Gislason, S.R., Arnorsson, S., 2001. Dissolution of primary minerals in natural waters:
774 II. Mineral saturation state. Chem. Geol. 172, 251–276.

775 Stoessell, R.K., 1988. 25 C and 1 atm dissolution experiments of sepiolite and kerolite. Geochim.
776 Cosmochim. Acta 52, 365–374.

777 Stoessell, R.K., Hay, R.L., 1978. The geochemical origin of sepiolite and kerolite at Amboseli, Kenya.

778 Contrib. to Mineral. Petrol. 65, 255–267. https://doi.org/10.1007/BF00375511

779 Strickland, J.D.H., Parsons, T.R., 1972. A practical handbook of seawater analysis. Fisheries research
780 board of Canada.

781 Teng, H.H., Dove, P.M., De Yoreo, J.J., 2000. Kinetics of calcite growth: surface processes and
782 relationships to macroscopic rate laws. Geochim. Cosmochim. Acta 64, 2255–2266.

783 Thom, J.G.M., Dipple, G.M., Power, I.M., Harrison, A.L., 2013. Chrysotile dissolution rates:
784 Implications for carbon sequestration. Appl. Geochemistry 35, 244–254.

785 Tipper, E.T., Galy, A., Gaillardet, J., Bickle, M.J., Elderfield, H., Carder, E.A., 2006. The magnesium
786 isotope budget of the modern ocean: constraints from riverine magnesium isotope ratios.
787 Earth Planet. Sci. Lett. 250, 241–253.

788 Tosca, N.J., Macdonald, F.A., Strauss, J. V., Johnston, D.T., Knoll, A.H., 2011. Sedimentary talc in
789 Neoproterozoic carbonate successions. Earth Planet. Sci. Lett. 306, 11–22.
790 https://doi.org/10.1016/J.EPSL.2011.03.041

791 Tosca, N.J., Masterson, A.L., 2014. Chemical controls on incipient Mg-silicate crystallization at 25°C:
792 Implications for early and late diagenesis. Clay Miner. 49, 165–194.
793 https://doi.org/10.1180/claymin.2014.049.2.03

794 Treguer, P., Nelson, D.M., Van Bennekom, A.J., DeMaster, D.J., Leynaert, A., Queguiner, B., 1995. The
795 silica balance in the world ocean: a reestimate. Science (80-.). 268, 375–379.

796 Tutolo, B.M., Tosca, N.J., 2018. Experimental examination of the Mg-silicate-carbonate system at
797 ambient temperature: Implications for alkaline chemical sedimentation and lacustrine
798 carbonate formation. Geochim. Cosmochim. Acta 225, 80–101.
799 https://doi.org/10.1016/j.gca.2018.01.019

800 Van Oosterwyck-Gastuche, M.C., La Iglesia, A., 1978. Kaolinite synthesis. II. A review and discussion
801 of the factors influencing the rate process. Clays Clay Miner. 26, 409–417.

802 Walther, J. V, Helgeson, H.C., 1977. Calculation of the thermodynamic properties of aqueous silica
803 and the solubility of quartz and its polymorphs at high pressures and temperatures. Am. J. Sci.
804 277, 1315–1351.

805 Wolery, T.J., Jove-Colon, C.F., 2004. Qualification of thermodynamic data for geochemical modeling
806 of mineral-water interactions in dilute systems.

807 Wolery, T.W., Jarek, R.L., 2003. Software user's manual. EQ3/6, version 8, 376.

808 Wollast, R., Mackenzie, F.T., Bricker, O.P., 1968. Experimental precipitation and genesis of sepiolite
809 at earth-surface conditions. Am. Miner. 53, 1645–1661.

810 Yalcin, H., Bozkaya, Ö., 2004. Ultramafic-rock-hosted vein sepiolite occurrences in the Ankara
811 Ophiolitic Melange, Central Anatolia, Turkey. Clays Clay Miner. 52, 227–239.

812 Yang, L., Steefel, C.I., 2008. Kaolinite dissolution and precipitation kinetics at 22 °C and pH 4.
813 Geochim. Cosmochim. Acta 72, 99–116. https://doi.org/10.1016/J.GCA.2007.10.011

814 Zhang, D., Zhou, C.-H., Lin, C.-X., Tong, D.-S., Yu, W.-H., 2010. Synthesis of clay minerals. Appl. Clay
815 Sci. 50, 1–11. https://doi.org/10.1016/J.CLAY.2010.06.019

816 Zhu, C., Blum, A.E., Veblen, D.R., 2004a. Feldspar dissolution rates and clay precipitation in the
817 Navajo aquifer at Black Mesa, Arizona, USA. Water-Rock Interact. 895–899.

818 Zhu, C., Blum, A.E., Veblen, D.R., 2004b. A new hypothesis for the slow feldspar dissolution in
819 groundwater aquifers. Geochim. Cosmochim. Acta 68, A148–A148.

820 Zhu, C., Lu, P., 2009. Alkali feldspar dissolution and secondary mineral precipitation in batch systems:

821 3. Saturation states of product minerals and reaction paths. Geochim. Cosmochim. Acta 73,
822 3171–3200.

823

824 Table 1. Compositions of the reactive inlet aqueous solutions. The ionic strength of the inlet
825 solutions are 0.02 M. Inlet solutions of the dissolution experiments are buffered to maintain a
826 constant pH. Inlet dissolution – 1 refers to the inlet solution to which no aqueous Si and Mg was
827 added, inlet dissolution – 2 refers to the reactive inlet solution of the dissolution experiment to
828 which Si and Mg was added. The headspace of the bottle in which the reactive inlet solution of the
829 growth experiments was stored, was constantly flushed with N_2 to maintain a constant pH.

	pH	***$Na_2SiO_3 \cdot 9H_2O$***	***$MgCl_2*6H_2O$***	***NH_4Cl***	***NH_3***	***NaCl***	***5M HCl***
		mmol/kgs	*mmol/kgs*	*mmol/kgs*	*mmol/kgs*	*mol/L*	*mmol/kgs*
Inlet precipitation	9.32	2.55	1.44			0.760	0.833
Inlet dissolution – 1	7.32			0.0224	0.964		
Inlet dissolution – 2	7.24	0.022	0.015	0.0224	0.964		

Table 2: Summary of the experimental results. The experiments labelled P-1 to P-6 represent the shorter-term growth experiments, while P-L gives the results of the longer-term growth experiment. Experiments D-1 to D-7 represent the shorter-term dissolution experiments. The dissolution experiments in which Mg and Si were added to the inlet solution are indicated by an Asterix. a_i represents the activity of the subscripted species and ΔMg^{2+} or ΔSi denote the average of the changes in Mg and Si concentration between the inlet and outlet fluids at steady state. The $\Delta Si/\Delta Mg$ values are based on the average ΔMg^{2+} or ΔSi in the experiments at steady state. Growth and dissolution rates reported here were computed using Eq. 4. Note that the rates in this table are reported as the logarithm of the absolute of the measured surface area normalized rates.

Exp. Name	*Flow rate*	*Surface area*	*Outlet pH*	a_{H+}	a_{Mg2+}	a_{SiO2}	ΔMg^{2+}	ΔSi	$\Delta Si/\Delta Mg$	$Log(r_+)$ *Si*	$Log(r_+)$ *Mg*
	g/s	m^2					*mmol/kgw*	*mmol/kgw*		$mol/s/cm^2$	$mol/s/cm^2$
P-1	2.81E-03	236	8.66	2.19E-09	1.12E-03	2.00E-03	0.219	0.217	0.99	-16.38	-16.26
P-2	9.02E-04	209	8.23	5.89E-09	1.67E-03	2.19E-03	0.254	0.298	1.17	-16.67	-16.55
P-3	1.32E-03	229	8.25	5.62E-09	8.13E-04	2.14E-03	0.210	0.371	1.76	-16.43	-16.52
P-4	7.64E-04	188	7.90	1.26E-08	7.94E-04	2.19E-03	0.285	0.399	1.40	-16.57	-16.22
P-5	5.50E-04	217	7.69	2.04E-08	1.21E-03	2.40E-03	0.134	0.258	1.92	-17.02	-17.08
P-6	4.87E-04	203	7.59	2.57E-08	1.65E-03	2.40E-03	0.185	0.299	1.62	-16.92	-16.93
P-L	6.68E-04	64.2	7.50	3.16E-08	9.13E-04	2.13E-03	0.301	0.352	1.17	-16.16	-16.07
D-1*	1.75E-04	162	7.74	1.82E-08	1.20E-04	2.76E-04	-0.108	-0.249	2.30	-17.34	-17.52
D-2	7.38E-04	171	7.63	2.34E-08	1.13E-04	2.64E-04	-0.0113	-0.264	2.33	-16.69	-16.87
D-3	1.68E-03	172	7.69	2.04E-08	8.04E-05	1.52E-04	-0.0756	-0.152	1.91	-16.58	-16.70
D-4	3.32E-03	167	7.83	1.48E-08	5.17E-05	9.66E-05	-0.0517	-0.0966	1.87	-16.50	-16.60
D-5*	1.43E-03	161	7.66	2.19E-08	8.34E-05	9.35E-05	-0.0737	-0.163	1.12	-16.60	-16.76
D-6	5.19E-03	164	7.85	1.41E-08	3.73E-05	7.42E-05	-0.0373	-0.0742	1.99	-16.38	-16.48
D-7	9.62E-03	170	7.94	1.15E-08	2.66E-05	4.94E-05	-0.0266	-0.0494	1.86	-16.34	-16.44

840

841 Table 3: Summary of the chemical affinity of sepiolite and the saturation indices (***SI***) in the reactive outlet solutions with respect to selected phases. The
842 experiments labelled P-1 to P-6 represent the shorter-term growth experiments, while P-L gives the results of the longer-term growth experiment.
843 Experiments D-1 to D-7 represent the shorter-term dissolution experiments. Saturation indices were obtained using PHREEQC. A positive chemical affinity
844 indicates that sepiolite is supersaturated, whereas a negative chemical affinity indicates that sepiolite is undersaturated.

Exp. Name	***A Sepiolite*** *kJ/mol*	***SI Sepiolite***	***SI SiO_2(am)***	***SI Forsterite***	***SI Talc***	***SI Chrysotile***	***SI Anthophyllite***	***SI Brucite***	***SI Kerolite***
P-1	89.94	14.11	-0.293	2.030	14.20	10.72	21.68	0.108	6.52
P-2	73.98	11.61	-0.253	0.699	12.30	8.74	17.20	-0.578	4.62
P-3	66.62	10.46	-0.263	0.148	11.45	7.91	15.23	-0.848	3.77
P-4	48.90	7.660	-0.256	-1.268	9.342	5.79	10.30	-1.559	1.66
P-5	44.44	6.973	-0.214	-1.697	8.805	5.17	8.991	-1.795	1.13
P-6	42.72	6.703	-0.214	-1.831	8.603	4.96	8.520	-1.862	0.924
P-L	29.57	4.640	-0.267	-2.757	7.082	3.549	5.041	-2.298	-0.598
D-1	-14.59	-2.287	-1.900	-5.703	-1.422	-1.688	-12.62	-2.955	-5.35
D-2	-21.58	-3.383	-1.724	-5.592	-0.814	-1.433	-11.44	-2.987	-7.28
D-3	-32.12	-5.037	-1.610	-5.273	-0.050	-0.898	-9.809	-2.885	-7.73
D-4	-36.75	-5.764	-1.411	-5.306	0.397	-0.847	-9.031	-3.001	-8.18
D-5	-40.67	-6.379	-1.169	-6.273	-0.449	-2.177	-11.33	-3.605	-8.42
D-6	-43.73	-6.859	-1.623	-5.553	-0.504	-1.324	-10.85	-3.018	-8.49
D-7	-49.65	-7.787	-1.154	-4.446	2.330	0.571	-4.863	-2.700	-9.10

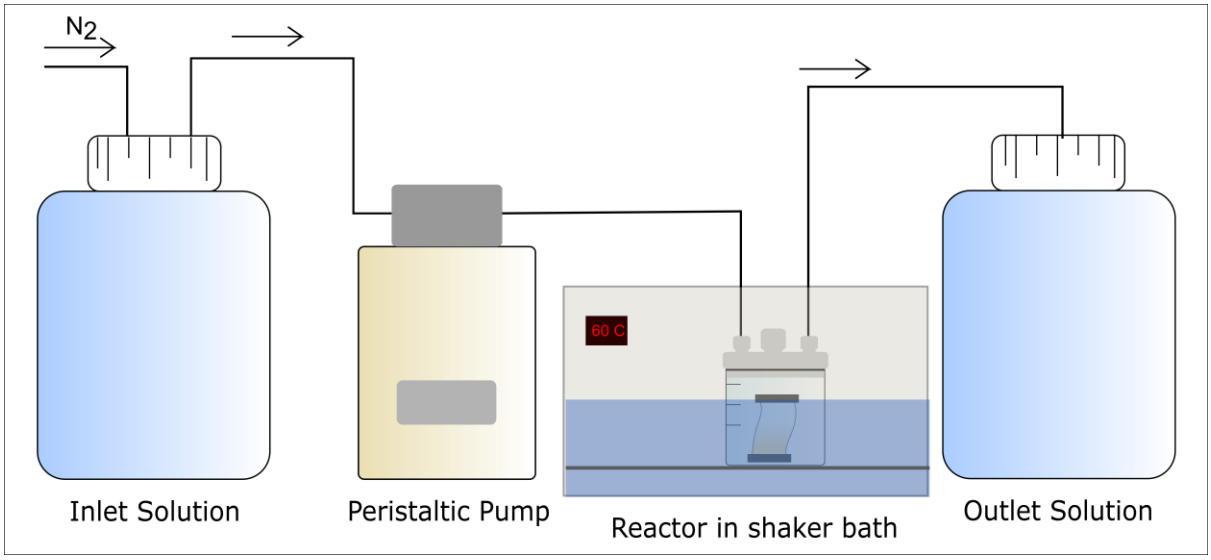

Figure 1. Schematic of the experimental reactor design. The reactor was placed in a 60 ^{o}C temperature controlled shaker bath. Sepiolite is contained in the reactor using a dialyses bag. Solutions are sampled from the outlet-line.

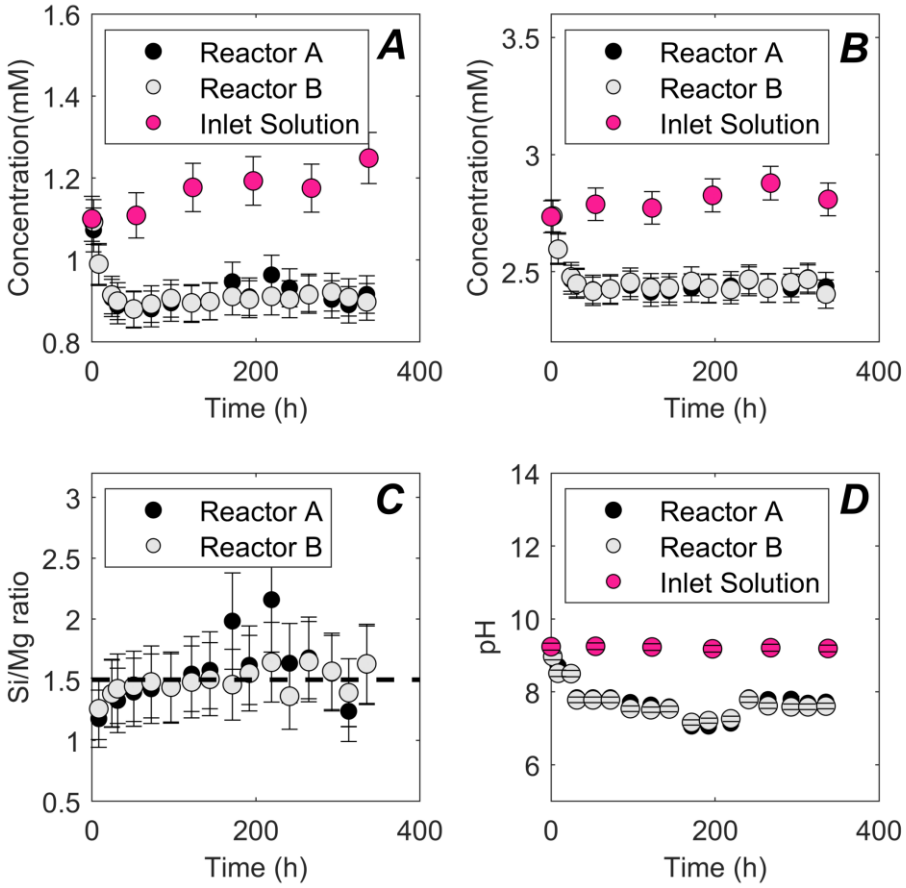

Figure 2. Temporal evolution of the reactive inlet and outlet solution compositions of experiment P-6. Figure A gives the aqueous Mg^{2+} concentrations over time, the grey and black symbols represent the results of the duplicate experiments. The pink symbols represent the Mg^{2+} concentrations in the inlet solutions. The error bars represent the uncertainty associated with the measurements. (B) The Si concentrations in the outlet of the duplicates (black and grey symbols) and the inlet solution (pink symbols). Figure (C) shows the ratio of the change in Si and Mg concentrations between the inlet and outlet solutions (ΔSi and ΔMg) during the experiments. The dashed line represents the common sepiolite molar Si/Mg ratio of 1.5. (D) Temporal pH evolution of the reactive outlet solutions of the duplicate outlet solutions (black and grey symbols) and the inlet solution (pink).

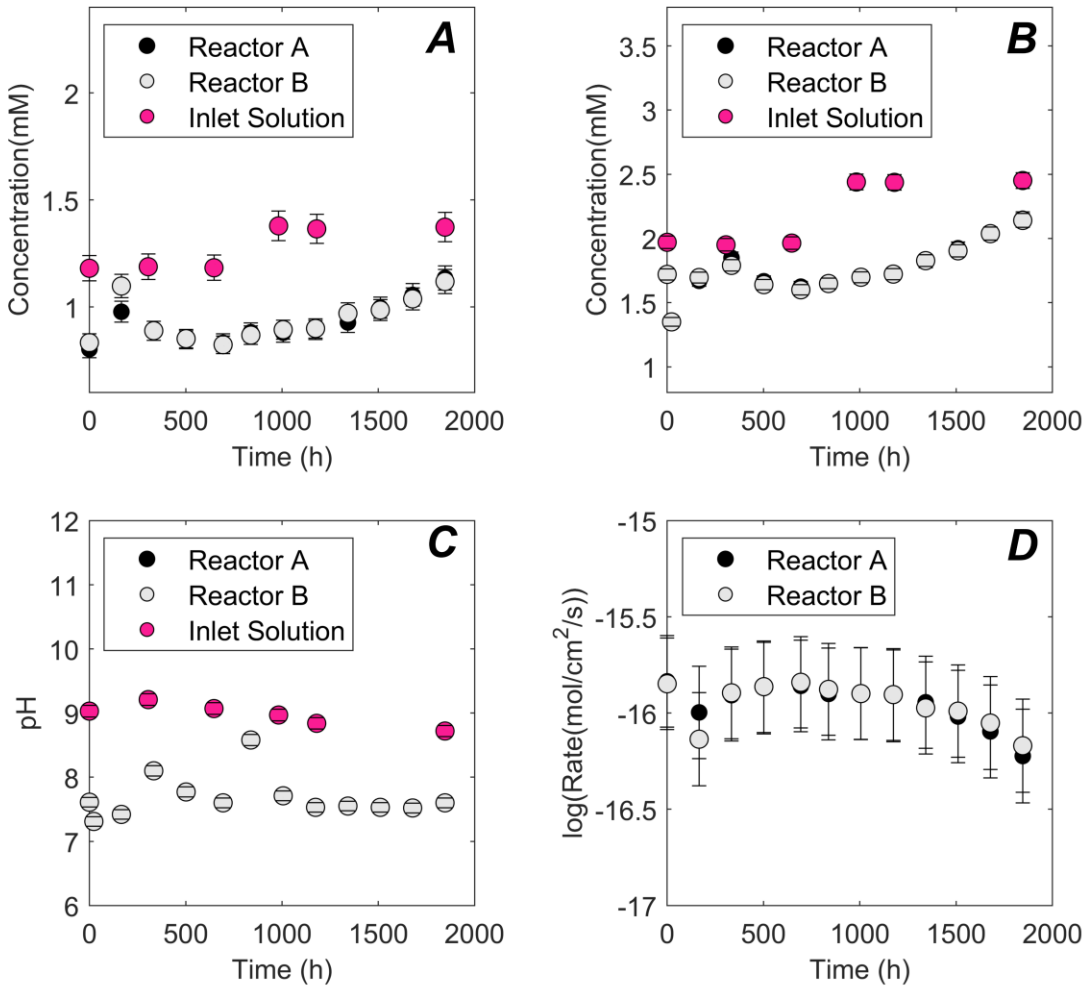

859 Figure 3. Results of the longer-term sepiolite growth experiments. Figure (A) gives the temporal
860 aqueous Mg concentrations, where the grey and black symbols represent the concentrations in the
861 duplicate outlet solutions, while the pink symbols represent the results of the concentrations in the
862 inlet solution. The error bars represent the uncertainty associated with the measurements. Figure
863 (B) shows the results of the aqueous Si concentrations. (C) pH. (D) the calculated precipitation rate
864 over time, based on the measured Mg concentrations.

865

866

867

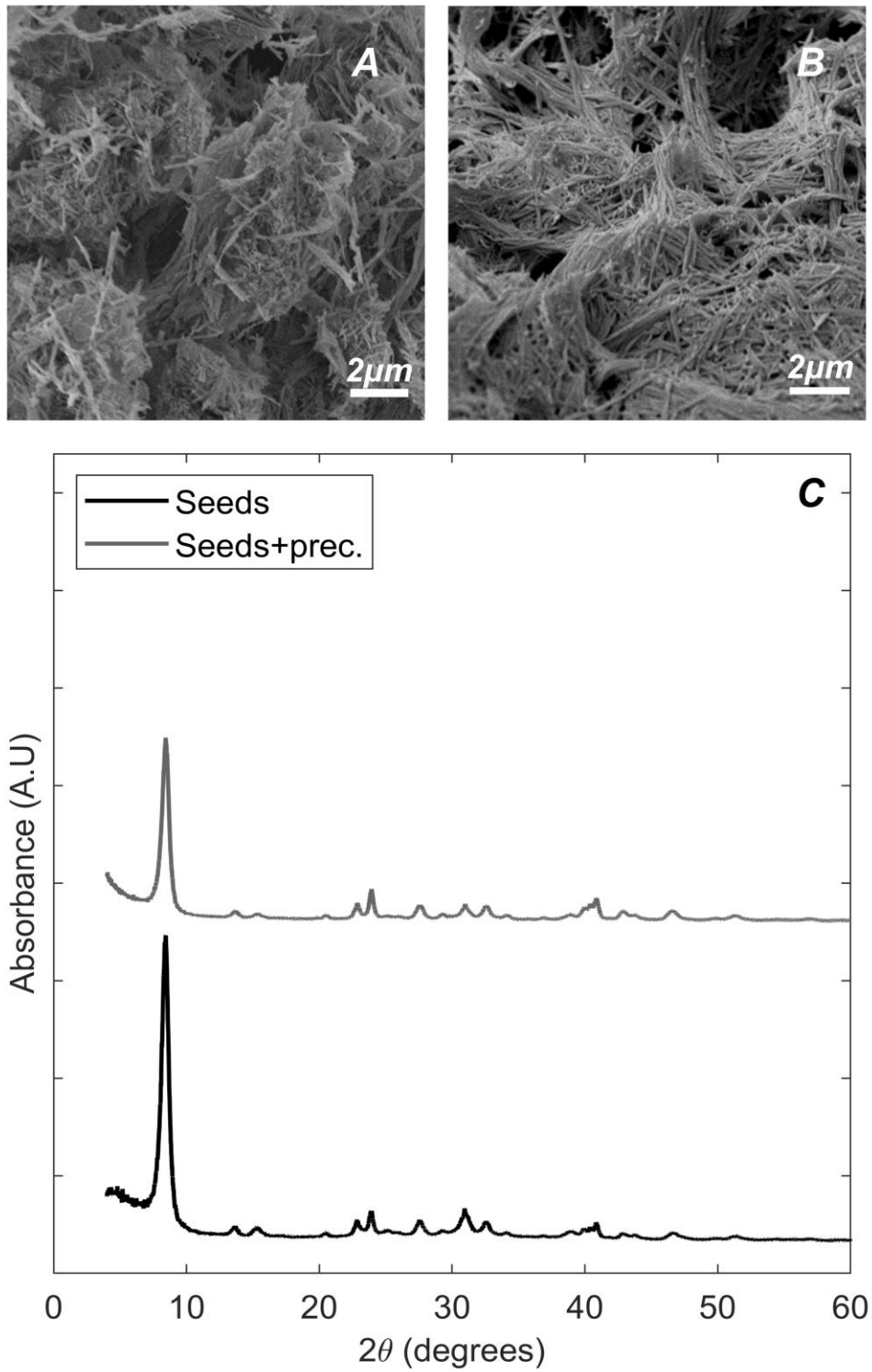

868

869 Figure 4. (A) SEM image of the sepiolite seed material. (B) SEM image of the solids collected
870 following the long-term growth experiments. Note that the morphology of the seed and the reaction
871 product are indistinguishable. (C) XRD diffractograms of the seed material and the post-experiment
872 solids after 2.5 months of growth. Note that diffractograms spectra indicate that the analysed phase
873 is pure sepiolite, suggesting the growth of crystalline sepiolite.

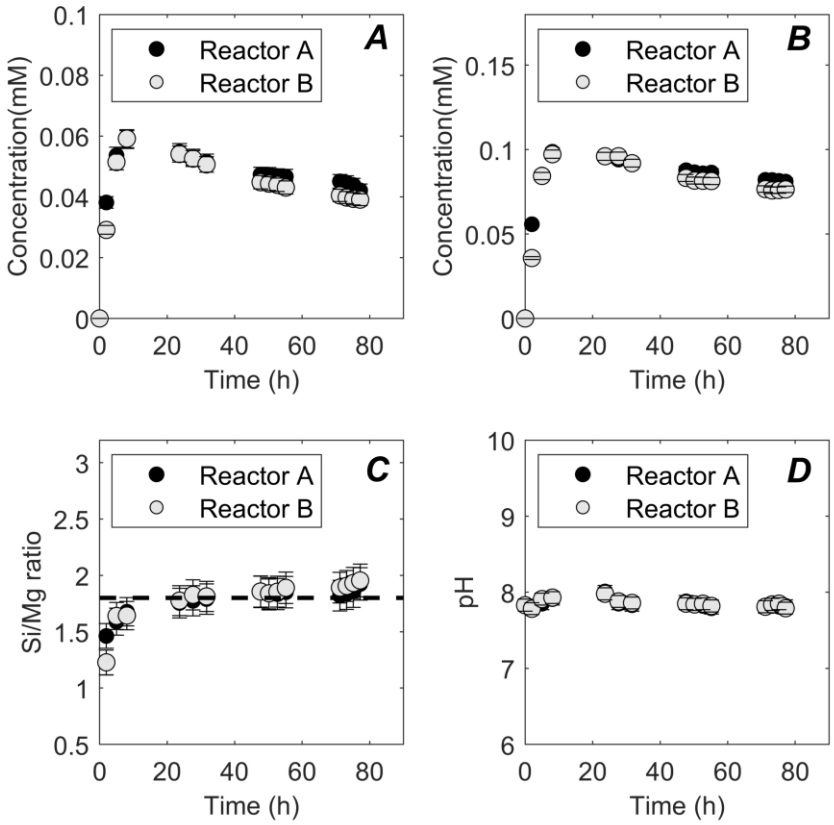

874 Figure 5. Representative temporal evolution of the sepiolite dissolution experiments (experiment D-
875 2). Figure (A) depicts the aqueous Mg^{2+} concentrations in the outlet solution over time, where the
876 grey and black symbols represent the results of the duplicate experiments. The error bars show the
877 uncertainty associated with these measurements. Figure (B) shows the results of the aqueous Si
878 concentration. (C) The ratio between molar Si/Mg in the outlet solution, where the dashed line
879 represents the composition of the sepiolite seed material used in these experiments, deviation from
880 this line thus represents non-stoichiometric dissolution. (D) The temporal pH evolution of the
881 experimental outlet solution in the duplicate experiments.

882

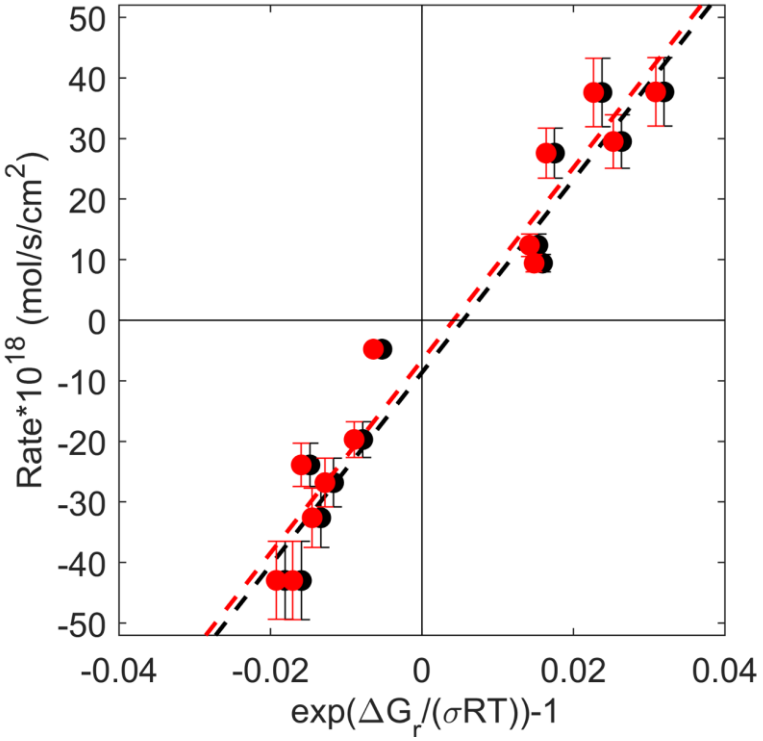

Figure 6. Relationship between $\exp\left(\frac{\Delta G_r}{\sigma RT}\right) - 1$ and sepiolite dissolution and growth rates. Negative rates denote the dissolution, while the positive rates represent the sepiolite growth. The dashed lines show a least squared linear fit of the data. The red symbols are computed using K_{sp} = $10^{27.66}$ (Christ et al., 1973) while the black symbols were computed using K_{sp} = $10^{27.17}$ (Wolery and Jove-Colon, 2004). Note that neither fit intercepts the origin.

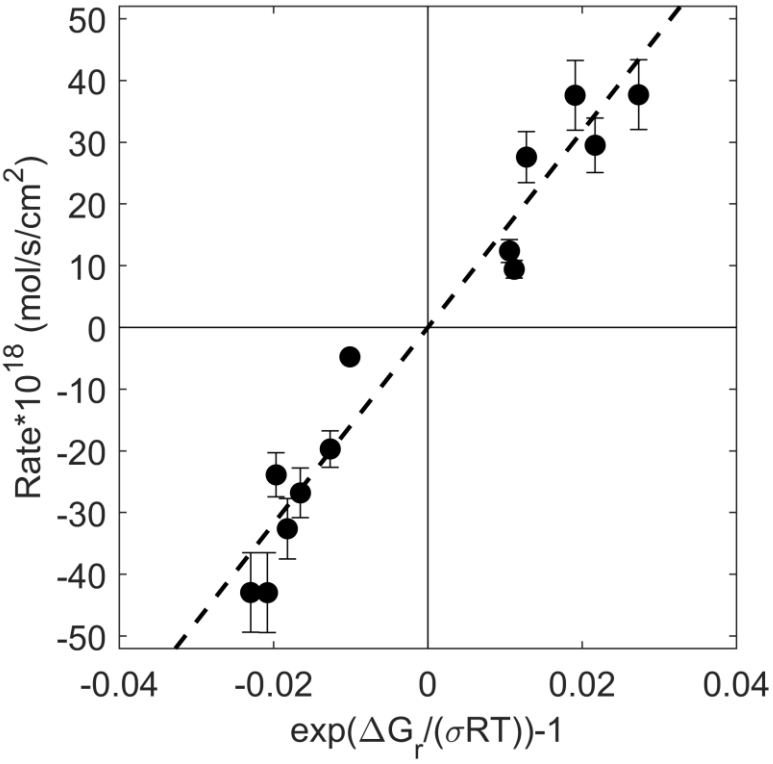

Figure 7. Relationship between $1 - \exp\left(\frac{\Delta G_r}{\sigma RT}\right)$ and sepiolite dissolution and growth rates. Negative rates correspond to dissolution, while the positive rates correspond to growth. The data was fit assuming that the rate of dissolution and precipitation is zero at chemical equilibrium. The chemical equilibrium constant associated with this fit, equals $10^{29.25\pm1.7}$.

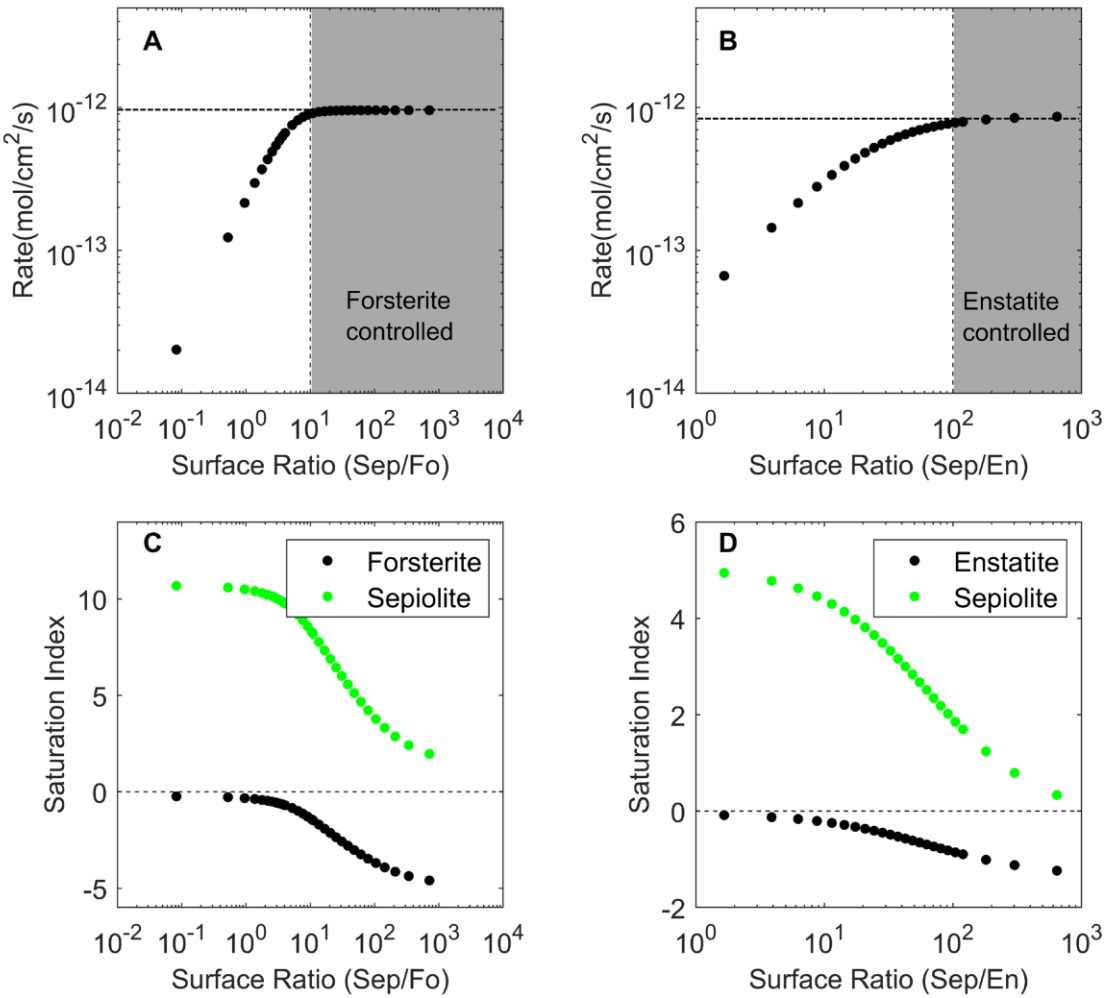

Figure 8. (A) Results of the computed relationship between forsterite (Fo) dissolution and sepiolite (Sep) growth rates as a function of the surface area ratio of Sep/Fo. The grey area depicts when the coupled rate is limited by forsterite dissolution. The dashed horizontal line depicts the far from equilibrium forsterite dissolution rates. (B) Results of the computed relationship between enstatite (En) dissolution and sepiolite (Sep) growth rates as a function of the surface area ratio of Sep/En. The rate of reaction increases when relatively more sepiolite is available. The grey area depicts when the coupled rate is limited by enstatite dissolution. The dashed horizontal line depicts the far from equilibrium enstatite dissolution rates. (C) The saturation indices of forsterite and sepiolite as a function of the sepiolite to forsterite surface area ratio. The saturation index of sepiolite is high when the surface area of sepiolite is high. Forsterite is close to chemical equilibrium when the surface area sites of sepiolite is relatively low slowing down dissolution rate. (D) The saturation indices of sepiolite and enstatite as a function of the sepiolite to enstatite surface ratio. Trends are similar as those observed in Figure C.

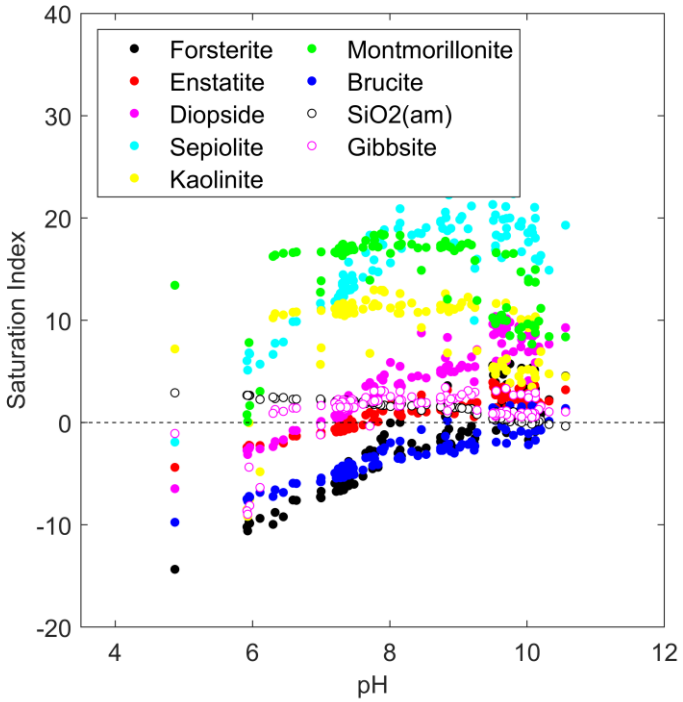

911

912 Figure 9. Computed saturation indices of several mineral in Iceland waters. The fluid compositions
913 were taken from Arnórsson et al. (1983), Gislason (1989), Gislason and Arnórsson (1993), Stefánsson
914 et al. (2001) and Stefánsson and Gislason, (2001). Note that primary minerals, such as forsterite,
915 enstatite and diopside approach equilibrium at pH ≥8, while clays are supersaturated at these
916 conditions. Metal oxides and amorphous SiO_2 are however close to equilibrium at these pH
917 conditions.